https://doi.org/10.5194/egusphere-2026-575
Preprint. Discussion started: 11 February 2026

AMOC weakening across latitude and time in CMIP6 future scenarios

Harry Ashton-Key[1,2], Jennifer Mecking[1], Robert Marsh[2], Sybren Drijfhout[2], Marilena Oltmanns[1,3,4], and Alejandra Sanchez-Franks[1]

[1]National Oceanography Centre, Southampton, UK
[2]University of Southampton, Southampton, UK
[3]Alfred Wegener Institute, Bremerhaven, Germany
[4]University of Bremen, Bremen, Germany

Correspondence: Harry Ashton-Key (hbak1n23@noc.ac.uk)

Abstract. The Atlantic Meridional Overturning Circulation (AMOC) is projected to weaken in the latest generation of climate models used in the Coupled Model Intercomparison Project, Phase 6 (CMIP6). There is uncertainty to the extent of weakening predicted, associated with model differences within the CMIP6 ensemble. The focus of this study is the latitudinal coherence of AMOC decline and how it differs between models and future forcing scenarios. AMOC weakening is presented as a function of latitude and time between 1900 and 2100 for depth-space and density-space. Weakening originates at high latitudes (45-47°N in depth-space and 51-61°N in density-space) and propagates southwards. As density-space weakening originates further north than depth-space, density-space is better suited for early warning signals. For density-space, the 25% weakening signal has an 11-year lag between 45°N and 26°N and in depth-space there is a 9-year lag. However, density-space has an additional 8-year lag between 57°N and 45°N giving a total lag of 19 years. As the AMOC weakens, the southward propagation of weakening (south of 40°N) slows with speeds ranging from 6.29 degrees per year to 0.40 degrees per year, dependent on model and scenario. Propagation speeds in depth-space and density-space are similar. In the strongest future forcing scenario, the propagation speed at 5% weakening is 2.78 degrees per year and at 30% weakening is 1.45 degrees per year. Also, the speed of southward propagation slows more intensely in less extreme climate change scenarios than in more extreme ones. As the AMOC weakens, the propagation speed of weakening is found to slow for some models while it remains constant for others. The CMIP6 models are categorised by whether the propagation speed is constant, declines to a constant, declines and increases again or continuously declines. The speed of propagation does not appear to be related to AMOC strength.

1 Introduction

The Atlantic Meridional Overturning Circulation (AMOC) is an important component of large-scale global ocean circulation. It is characterised by northward flow of warm and salty surface water, densification of water at high latitudes and the southward return flow of colder, fresher deep water. Europe's mild climate is due to the AMOC transporting heat northward, it is responsible for 0.5 PW of cross-equatorial heat transport (Trenberth and Fasullo, 2017) and 1.2 PW northward heat transport at 26.5°N (Johns et al., 2023).

https://doi.org/10.5194/egusphere-2026-575
Preprint. Discussion started: 11 February 2026

The latest generation of climate models in the Coupled Model Intercomparison Project, phase 6 (CMIP6) (Eyring et al., 2016) predict the AMOC will weaken on average by 24-39% by 2100 dependent on future scenario (Weijer et al., 2020; Fox-Kemper et al., 2021). A weakened AMOC will have significant weather and climate risk for Europe such as an increased risk of heatwaves (Meccia et al., 2025), although they may be less severe with a weakened AMOC (Duarte et al., 2025), enhanced storm tracks over Northwestern Europe (van Westen and Baatsen, 2025; Vacca et al., 2025) and lagged warming compared to the rest of the world (van Westen and Baatsen, 2025; Vacca et al., 2025). On top of the localised impacts, there are a variety of global climate impacts to a weakened AMOC (e.g. changes to precipitation patterns (Bellomo et al., 2021; Jackson et al., 2015), reduced northern hemisphere temperatures (Jackson et al., 2015; Liu et al., 2020) and a poleward shift of northern hemisphere midlatitude jets (Liu et al., 2020; Bellomo et al., 2021)). There are, however, large uncertainties on the magnitude of AMOC weakening linked to model differences between the CMIP6 ensemble, e.g. due to mean state AMOC strength (Jackson et al., 2020; Lin et al., 2023), connectivity between the Atlantic and Indo-Pacific (Baker et al., 2023) and parametrisation schemes (Zhao et al., 2024). Improved understanding of the model differences could be used to improve model simulations, constrain existing AMOC projections and increase confidence in predictions of future impacts.

A general mechanism for AMOC weakening under climate change was proposed by Levang and Schmitt (2020): freshening of the surface layer occurs due to changes in the water cycle, the fresh layer inhibits heat exchange with the atmosphere, preventing cooling, and results in a subsurface warm 'blob'. The warm blob increases stratification across the surface, reducing the formation of North Atlantic Deep Water (NADW) and slowing the overturning circulation. This occurs in the subpolar North Atlantic in the marginal seas of deep water formation, namely the Labrador, Irminger and Nordic seas. There are numerous studies on AMOC decline in CMIP6, typically using an AMOC index at specific latitudes such 26.5°N, the latitude of the RAPID array (Weijer et al., 2020; Bryden et al., 2024; Madan et al., 2023). However, the latitudinal structure of AMOC weakening and possible differences across CMIP6 future projections are poorly understood.

Latitudinal connectivity of the AMOC is an active area of research, particularly regarding the propagation of density anomalies and understanding multi-decadal variability. The timescale of interest plays a key role in understanding the meridional coherence of the AMOC. Fast connectivity of density anomalies between the subpolar and subtropical gyres (with the subtropical lagging the subpolar on the order of 1-2 years) has been found by studying observational arrays (Wett et al., 2023; Han, 2023). Coherence between the Labrador Sea and the subtropical gyre has also been assessed in model studies, showing a lag in density anomalies on the order of 3-4 years (Zhang, 2010; Zou et al., 2019; Kostov et al., 2022) while others show a lag of between 5-10 years, a result that is model dependent (Li et al., 2019). One potential reason for this difference is the resolution of the models. Higher resolution models that resolve eddies have been shown to propagate tracer (e.g. salinity) signals faster along the Deep Western Boundary Current (DWBC) than in non-eddying models (Weijer et al., 2012). Models that do not resolve eddies and the Rossby deformation radius struggle to accurately capture propagation speed along the boundary (Marshall and Johnson, 2013) and parameterisation in coarse resolution models could explain differences in propagation speed. The presence of eddies in models has also been shown to impact the rate and severity of AMOC decline due to freshwater hosing (Den Toom et al., 2014; van Westen et al., 2025). Most CMIP6 ocean models have (nominally) 1 degree resolution and do not resolve eddies but some modelling centres provide higher resolution versions.

Zhang (2010) propose advection by mean flow of density anomalies and by coastal Kelvin waves as the main mechanisms by which density anomalies are transported north of 35°N. The relationship between changes to densification in the SPG and AMOC strength south of the SPG (at 45°N) was the subject of a recent modelling study by Petit et al. (2025), where the authors found coherence was facilitated by the shoaling of isopycnals along the DWBC resulting in changes to the zonal density gradient. This response occurs on the order of months. They also noted no coherence between AMOC strength between the OSNAP arrays and 45°N. The role wind plays in the connectivity of the AMOC is complex, with Zou et al. (2019) highlighting that meridional coherence can be driven by wind forcing as well as by buoyancy forcing while Fraser et al. (2025) discuss that wind driven Ekman pumping can disrupt meridional coherence in both depth and density-space representations of the AMOC.

The AMOC responds to high latitude buoyancy forcing on many time scales, from months and years to slow adjustments to the mean state on multi-decadal timescales (Gu et al., 2020). Proposed mechanisms that facilitate this adjustment include the slow advection of anomalies along the western boundary (Gerdes and Köberle, 1995; Hodson and Sutton, 2012; Zhao et al., 2017), or a baroclinic adjustment of the ocean interior from Rossby waves mediated by equatorial Kelvin waves (Döscher et al., 1994; Marshall and Johnson, 2013). The decadal changes to the structure of the AMOC in response to climate change, rather than annual variability of density anomalies, is the focus of this study.

The AMOC can be represented by overturning streamfunctions in depth-space, with latitude-depth coordinates, and in density-space, with latitude-density coordinates. The depth-space AMOC best represents vertical mass flux while the density-space AMOC better captures water mass transformation, particularly at high latitudes (Hirschi et al., 2020). The depth-space AMOC is more straightforward to compute and has historically been used more commonly than the density-space AMOC. Density-space AMOC has gained popularity because of its description of water mass transformation, particularly in the subpolar North Atlantic (Buckley et al., 2023; Straneo, 2006; Pickart and Spall, 2007). Propagation differences of weakening between a depth-space and density-space were explored by Kwon and Frankignoul (2014) considered in the context of a 20 year cycle of AMOC variability and showed at depth a broadly southward propagation of weakening for both representations.

The focus of this study is to understand the latitudinal and basin-wide changes to the AMOC under CMIP6 future scenario forcing, both in the multi-model mean and individual models, and to understand how weakening signals propagate through the basin. This study uses a new technique to investigate latitudinal connectivity of AMOC weakening using exclusively the streamfunction. Specifically, we consider the AMOC decline across the basin rather than at select latitude to deliver new insights into the latitudinal connectivity of AMOC weakening for the CMIP6 model set. The analysis is split into three sections. The first section is on the differences of AMOC weakening and propagation speed in depth-space and density-space representations of the AMOC, using the multi-model mean and the ssp585 experiment. The second section is on the differences of the basin-wide response between future climate forcing scenarios of the multi-model mean. The third section explores individual model differences of the propagation speed of weakening and categorises models according to those differences.

https://doi.org/10.5194/egusphere-2026-575
Preprint. Discussion started: 11 February 2026

2 Methods and Data

2.1 CMIP6 Models

This study analyses data from 15 models from the Coupled Model Intercomparison Project Phase 6 (CMIP6) (Eyring et al., 2016). Historical experiments, using historical external forcing, simulating 1850 to 2014 (Eyring et al., 2016) and four ScenarioMIP future projections for 2015-2100 (O'Neill et al., 2016); ssp126 (low emission), ssp245 (medium emission), ssp370 and ssp585 (high emission) are investigated. One ensemble member was used for each of the CMIP6 models in this study and are listed in Table 1. Since the focus of this study is the AMOC streamfunction the models selected require either the monthly-resolution depth- and density-space streamfunctions available or have the necessary variables to compute them: meridional mass transport (vmo) or meridional velocity (vo) as well as practical salinity (so) and potential temperature (thetao) for the historical and all the previously mentioned ScenarioMIP experiments. These requirements limit the number of models available to use in this study to 15.

Model	Institution	Variables	Ensemble Member	References
ACCESS-CM2	CSIRO	msftmz msftmrho	r1i1p1f1	(Bi et al., 2020)
ACCESS-ESM1-5	CSIRO	msftmz msftmrho	r1i1p1f1	(Ziehn et al., 2020)
CanESM5	CCCma	vmo vo, so, thetao	r1i1p1f1	(Swart et al., 2019)
CAS-ESM2-0	CAS	msftmz vo, so, thetao	r1i1p1f1	(Zhang et al., 2020)
CESM2-WACCM	NCAR	msftmz vo, so, thetao	r1i1p1f1	(Danabasoglu et al., 2020)
CMCC-ESM2	CMCC	vmo vo, so, thetao	r1i1p1f1	(Lovato et al., 2022)
CNRM-CM6-1	CNRM-CERFACS	vmo vo, so, thetao, thkcello	r1i1p1f2	(Voldoire et al., 2019)
EC-Earth3	EC-Earth-Consortium	vmo vo,so,thetao,thkcello	r1i1p1f1	(Döscher et al., 2022)
EC-Earth3-Veg-LR	EC-Earth-Consortium	vmo vo, so, thetao, thkcello	r1i1p1f1	(Döscher et al., 2022)
IPSL-CM6A-LR	IPSL	vmo vo,so,thetao,thkcello	r1i1p1f1	(Boucher et al., 2020)
MIROC6	MIROC	msftmz vo, so, thetao	r1i1p1f1	(Tatebe et al., 2019)
MRI-ESM2-0	MRI	msftmz msftmrho	r1i1p1f1	(Yukimoto et al., 2019)
NorESM2-LM	NCC	msftmz msftmrho	r1i1p1f1	(Seland et al., 2020)
UKESM1-0-LL	MOHC	msftyz vo, so, thetao, thkcello	r1i1p1f2	(Sellar et al., 2019)
TaiESM1	AS-RCEC	vo vo, so, thetao	r1i1p1f1	(Wang et al., 2021)

Table 1. The CMIP6 models used this study, listed with their institution, the variables and the ensemble member used. Streamfunctions provided by the modelling centres are labelled "msftmz" or "msftyz" for depth-space and "msftmrho" for density-space. Calculated streamfunctions are labelled by the variables they are calculated with: "vmo" (meridional mass transport) or "vo" (meridional velocity) for depth-space and "vo", "so" (absolute salinity), "thetao" (conservative temperature) and when available "thkcello" (variable vertical thickness) for density-space.

2.2 AMOC Streamfunction

Only eight of the models in this study had the depth-space streamfunction available (see Table 1 for labels "msftmz" or "msftyz"). When the depth-space AMOC streamfunction was not available, it was computed with Eq. (1) using the meridional mass transport ("vmo") and converted to volume transport using a reference water density of 1026 kgm^{-3}. For TaiESM1, the mass transport was not available and instead volume transport was calculated with the meridional velocity ("vo") and model grid dimensions.

The depth-space streamfunctions were calculated by the integral as described in (Hirschi and Marotzke, 2007), modified for mass transport,

$$\psi_z(y,z',t) = \frac{1}{\rho_0}\int_{x_w}^{x_e} dx \int_{-H(x,y)}^{z'} (vmo(x,y,z,t) - \widehat{vmo}(y,t))dz \tag{1}$$

where $\psi_z(y,z',t)$ is the streamfunction, ρ_0 is a reference water density of 1026 kgm^{-3}, vmo is the meridional mass transport, $\widehat{vmo}$ is the section averaged mass transport as a correction term for mass conservation,

$$\widehat{vmo}(y,t) = \frac{1}{A(y)}\int_{x_w}^{x_e}\int_{-H(x,y)}^{z_{surf}} vmo(x,y,z,t)dxdz \tag{2}$$

where $A(y)$ is the section area at a given latitude y. $H(x,y)$ is the bottom topography, x is longitude with x_e and x_w as the eastern and western boundary, y is latitude, z_{surf} is surface and t is time.

Only four modelling centres provided the density-space streamfunction, compared to eight modelling centres that provided the depth-space (see Table 1 for the label "msftmrho"). Calculating the density-space streamfunction requires the density at every grid point. Practical salinity ("so") and potential temperature ("thetao") are interpolated from the model T-grid points to the model V-grid points and sigma-2 density was calculated using the Gibbs SeaWater (GSW) Oceanographic Toolbox for python (McDougall and Barker, 2011). Sigma-2 is density referenced to 2000 dbar using the TEOS-10 (IOC et al., 2010) equation of state.

The density-space streamfunctions were calculated with the integral,

$$\psi_\rho(y,\rho',t) = \int_{x_w}^{x_e} dx \int_{-H(x,y)}^{\rho'} v(x,y,\rho,t)d\rho \tag{3}$$

where $\psi_\rho(y,\rho',t)$ is the streamfunction, v is the meridional velocity component, $H(x,y)$ is the bottom topography, x is longitude, y is latitude, ρ' is variable density and t is time. The density-space streamfunctions were calculated as in Eq. (3) using the NEMO Cookbook python package (Tooth, 2026). The densities in sigma-2 were binned over the range of 28-38 kg m^{-3} in 0.125 kg m^{-3} bins. All calculations, for depth and density, were done on the v-grid points of the native model grid.

2.3 AMOC Strength and Weakening

For this study the AMOC strength is defined at each latitude in the Atlantic as the maximum of the overturning streamfunction measured in Sverdrups (1 Sv $\equiv 10^6$ m^3s^{-1}) for both the depth- and density-space AMOC. The latitudinal response of the AMOC is investigated over the Atlantic basin (30°S to 65°N). To avoid the wind driven cell, AMOC strength computation excludes the top 500 m in depth-space and excludes densities less than 35.5 kgm^{-3} in density-space.

The response of the AMOC to future climate change scenarios is calculated as the percentage reduction from a historical reference period (1850-1899). The multi-model mean (MMM) AMOC strength for the historical reference period in depth-space has a peak AMOC strength of 18.2 Sv (at 35°N) and a minimum strength south of the peak of 14.8 Sv (at the equator) (Fig. 1a) while in density-space the peak AMOC strength is 18.0 Sv (at 55°N) and the minimum strength south of the peak of 14.0 Sv (at 30°S) (Fig. 1b). A 50-year period has been chosen for the reference period to reduce the impacts of interannual and multi-decadal variability.

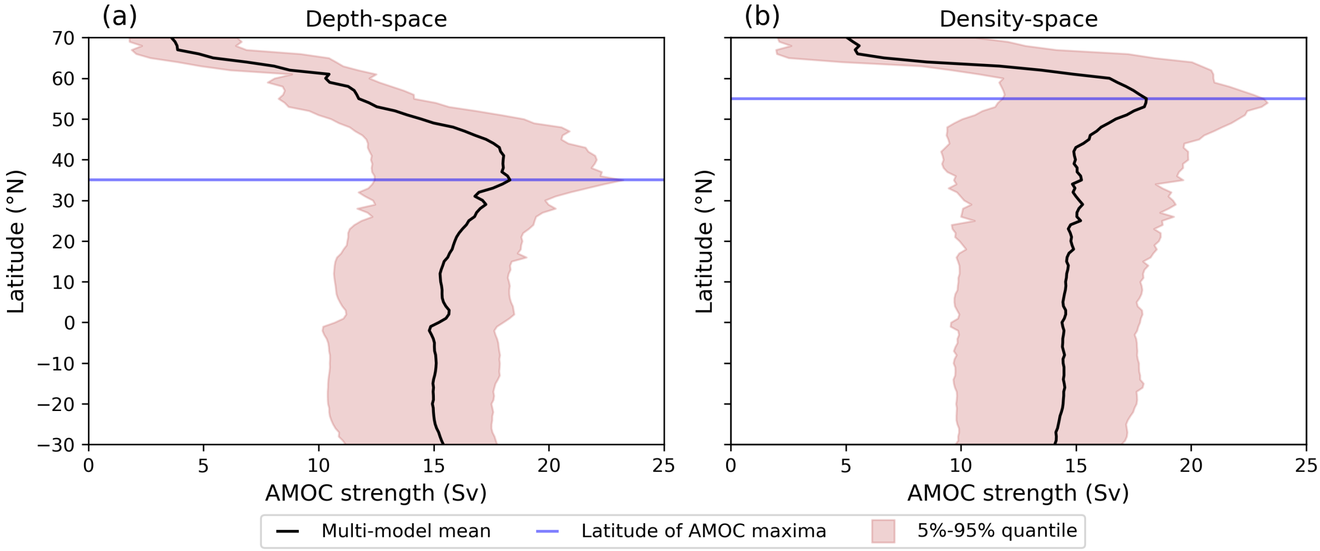

Figure 1. Average AMOC strength over the historical period 1850-1899 for depth-space (a) and density-space (b) as a function of latitude. Black lines show the multi-model mean. The blue lines highlight the latitude of the MMM streamfunction maximum. The red shading shows the 5%-95% quantile range of the reference strengths for the model set. Note the substantial drop in AMOC strength north of 65°N in both representations.

AMOC strength is calculated as a 10-year running mean from 1900-2100 for the historical and four future scenarios and are labelled as the centre year of the decade, providing "annual" AMOC strengths from 1905 to 2095. The percentage weakening is computed relative to the reference period at each latitude. Latitudes are resampled onto a regular 1-degree resolution grid from 30°S to 65°N for consistency across the models. Changes to the streamfunctions north of 65°N are not considered due to the weak mean streamfunction and curved model grids at these latitudes.

AMOC weakening refers to the reduction AMOC strength relative to the reference period. Thus, a negative AMOC weakening indicates a strengthening of the AMOC relative to the reference period. The use of percentage weakening rather than absolute reduction (in Sverdrups) is to allow the direct comparison of weakening between models that have a wide range of AMOC strengths, as is evident in the quantile ranges seen in Fig. 1. Taken at the multi-model mean peak (35°N for depth-space, 55°N for density-space), AMOC strength ranges from 12.0 Sv (CanESM5) to 23.8 Sv (TaiESM1) and from 11.5 (CanESM5) Sv to 24.7 Sv (TaiESM1) for depth- and density-space respectively.

2.4 Threshold Weakening

To connect AMOC weakening across latitudes, contours are computed at specific percentages of weakening, henceforth referred to as weakening thresholds or threshold. The first year a given weakening threshold is exceeded is recorded at each latitude. The threshold line is defined for a specific weakening threshold, e.g. 15%, as the contour of years as it changes across latitudes. The latitude at which the threshold is first exceeded indicates the year where AMOC weakening originates. The weakening anomaly of a given threshold can be followed throughout the basin to paint a picture of its propagation. The threshold lines are calculated at 2.5% intervals over the range 2.5%-60% between the 2000-2095.

The gradient of the threshold line represents the speed of propagation of the AMOC weakening signal at a specific percentage reduction. The larger the gradient, the faster the signal is transported southward. Assuming the threshold lines are approximately linear, the "weakening gradient" is found by performing a linear least-squares regression between 40°N and 30°S. This latitude range is chosen to capture the propagation south of the weakening onset. To ensure confidence in the validity of the gradient for a given threshold there must be at least a continuous line of thresholds from 40°N to the equator. This prevents erroneous gradients arising from limited data points. With these criteria the linear fits of all models, with the exception of MIROC6, have a mean p-value < 0.05 and all models, with the exception of EC-Earth3, have an mean absolute r-value > 0.8 for all four scenarios.

When comparing differences between future scenarios, the significances are computed using a two sided student t-test and a p-value of 0.05.

3 Results

The results are presented in three sections: differences in AMOC weakening between the depth-space and the density-space representation in the ssp585 experiment (Sect. 3.1), comparisons of weakening across four ScenarioMIP experiments (Sect. 3.2) and different weakening behaviours across the CMIP6 models used in this study (Sect. 3.3).

3.1 Depth-space and density-space

The MMM reference streamfunctions for depth-space (Figs. 1a,2a) and density-space (Figs. 1b,2b) respectively show peak overturning at 35°N and 55°N. By the end of the 21st century both streamfunctions have shoaled and weakened in amplitude (Figs. 2c and 2d). The streamfunction maxima are now at 30°S for both representations and there is no longer a clearly

https://doi.org/10.5194/egusphere-2026-575
Preprint. Discussion started: 11 February 2026

defined latitudinal maxima in the North Atlantic. Taking the difference between the reference streamfunction and the ssp585 streamfunction confirms that the greatest reduction in the AMOC occurs where the AMOC is strongest in the reference (Figs. 2e and 2f). Figure 2f also shows an increase in the density-space streamfunction at the lightest densities north of 40°N. This increase is due the surface waters in the SPG becoming less dense due to subsurface warming (Lin et al., 2023; Levang and Schmitt, 2020), so it is not that the streamfunction has strengthened but instead the density classification has shifted. The standard deviations of the differences reveal that the largest spread is not aligned with maximum weakening (Figs. 2g and 2h). Instead, the greatest standard deviations are on the contours above and below the peak. This could indicate the model spread is most strongly determined by the intensity of shoaling and change in vertical position of the AMOC streamfunction as it weakens. This relates to a recent study that found models with deeper AMOCs exhibit greater shoaling than with shallower AMOCs and these models with deeper AMOCs may be more sensitive to warming than observations imply (Bonan et al., 2025).

With only two snapshots in time, Fig. 2 provides limited insight to how the AMOC changes latitudinally in time. It shows the greatest weakening is concentrated in the North Atlantic and the least weakening occurs closer to the southern boundary of the South Atlantic but there is no detail on the connectivity. The processes driving AMOC weakening occur at high latitudes in the SPG and it makes sense for weakening to be greatest at the high latitudes but it is unclear from Fig. 2 if the severity of weakening at high latitudes is or will be reflected by AMOC changes further south. By representing AMOC weakening as a function of latitude and time, the connectivity of AMOC weakening across the Atlantic basin is revealed and the timescales of AMOC weakening can be inferred. Figure 3 shows the percentage weakening Hovmöllers for depth-space and density-space plots from the first decade after the reference period (1905) to the end of the ssp585 experiment (2095). Changes from 1905-2000 are not of particular interest to this study but are included for completeness. This time period does show AMOC strengthening between 1960-2000 of approximately 10% in both depth and density space, attributed to aerosol emissions (Menary et al., 2020), before the AMOC starts declining from 2015.

AMOC weakening begins at high latitudes, north of 40°N, with a slow propagation of the weakening signal to the southern boundary of the Atlantic basin in both depth-space and density-space (Fig. 3a and Fig. 3b). This is clearest when following the threshold lines. The latitude of onset is further north in density-space than depth-space, as expected when looking at the streamfunctions (Kwon and Frankignoul, 2014) due to the density streamfunction taking into account changes in the zonal structure in higher latitude North Atlantic, which are suppressed in the depth-space streamfunction. In both depth and density space representations of the AMOC streamfunction there is a slight southward shift of the onset latitude as the threshold increases, 47°N to 45°N in depth-space and 61°N to 51°N in density-space from 5% threshold to 45% threshold. The difference between onset latitudes means density-space shows AMOC weakening earlier than in depth-space. For example, the 25% threshold reached in 2035 in density-space compared to 2047 in depth-space. South of 40°N the timings of the threshold lines realign between the two representations.

Relating Fig. 3 to the latitudes of the observational arrays RAPID (26°N, (Smeed et al., 2014)) and OSNAP (53-60°N, (Lozier et al., 2017), where we use 57°N to represent the whole array) reveals that for thresholds over 10%, weakening at OSNAP precedes weakening at RAPID by at least a decade (10-22 years) in density-space while only precedes by 4-11 years

https://doi.org/10.5194/egusphere-2026-575
Preprint. Discussion started: 11 February 2026

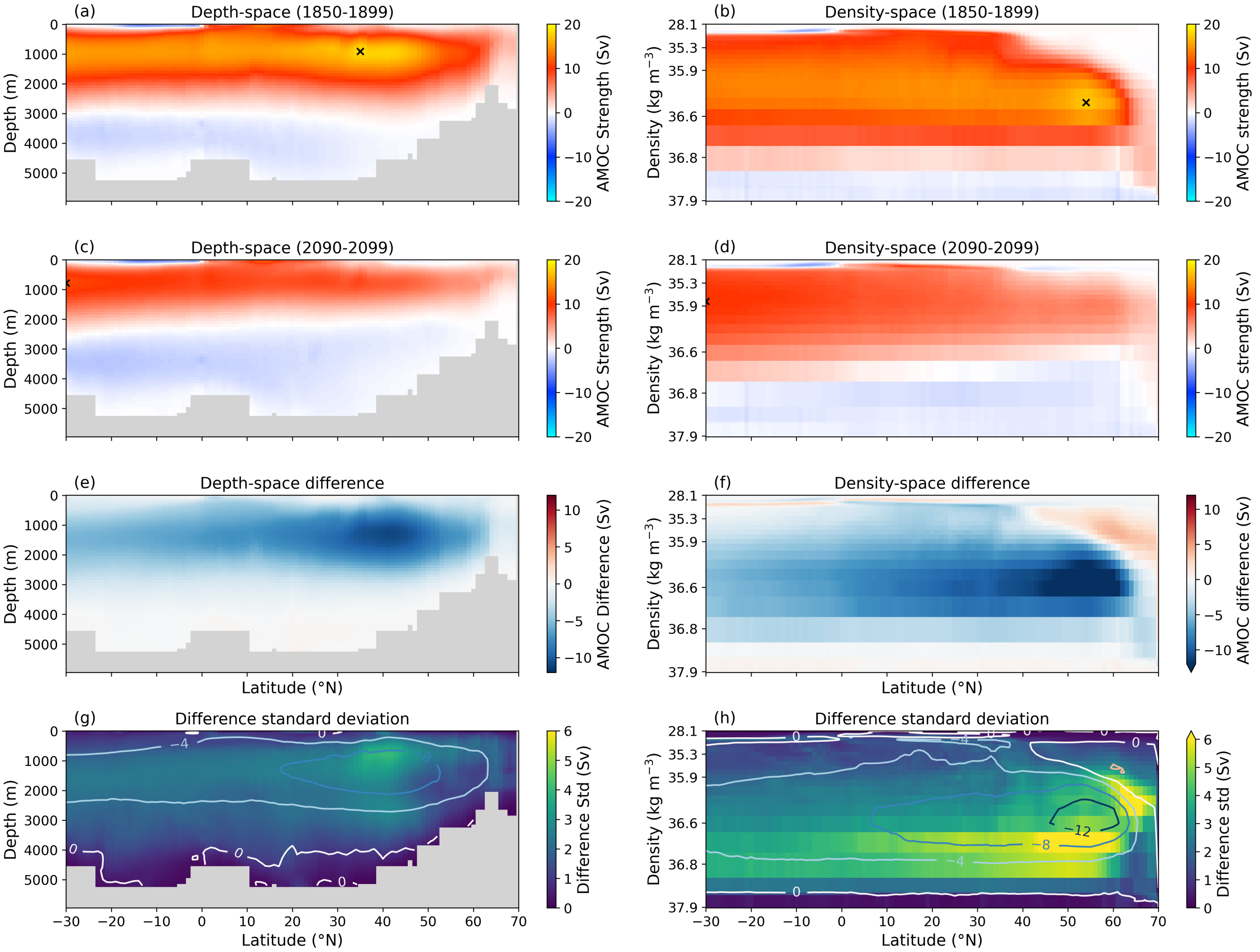

Figure 2. Multi-model mean depth-space (left column) and density space (right column) streamfunctions. (a,b) Averaged over the historical reference period (1850-1899). (c,d) Averaged over the last decade of the ssp585 scenario (2090-2099). The maxima of the streamfunctions are marked by 'x'. (e) The difference between (a) and (c). (f) The difference between (b) and (d). (g,h) the standard deviations of the differences (e,f) contoured with the differences. Note the non-linear vertical scale in the density plots. Topography in depth-space is the aggregation of all model topographies.

in depth-space. As an illustrative example, we consider the difference in detection time of 25% weakening at OSNAP and RAPID in depth-space and density-space. In density-space, OSNAP precedes RAPID by 19 years for ssp585 (ranging over 210 19-22 years, depending on scenario). In depth-space, OSNAP precedes RAPID by only 4 years for ssp585 (ranging over 3-5 years, depending on scenario). Since the onset latitudes of AMOC weakening in depth-space are further south than the OSNAP array, there are delays in detection at OSNAP when compared to the detection of weakening in density-space, where the onset

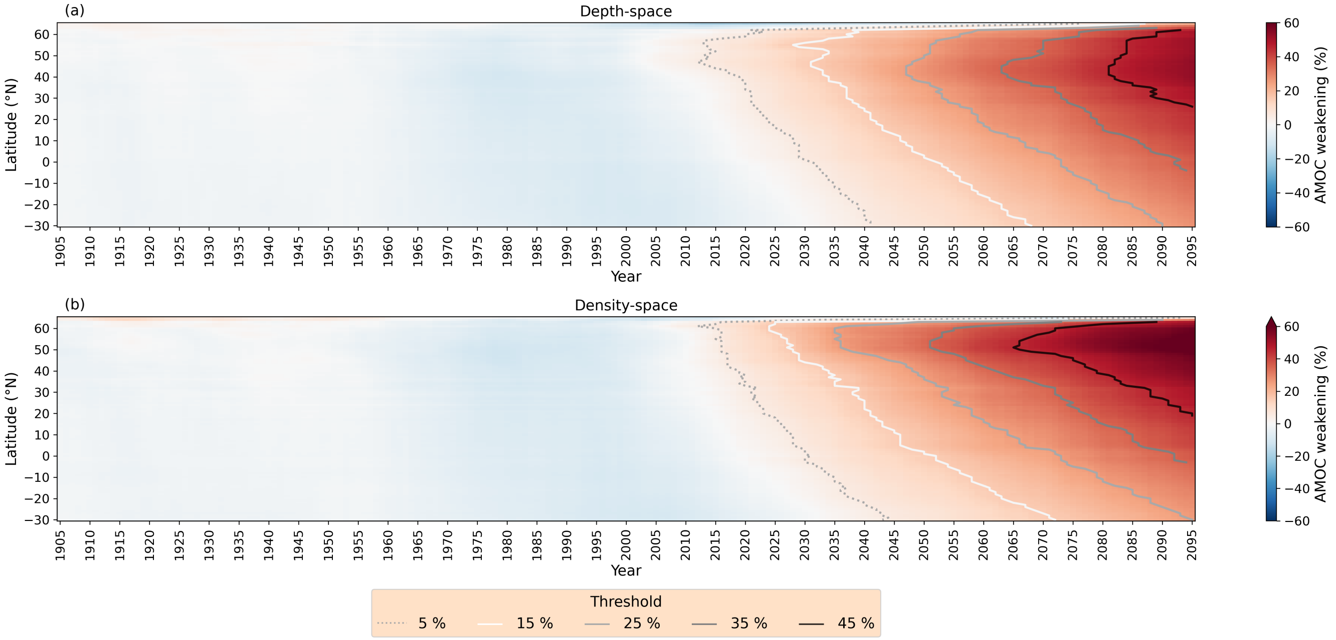

Figure 3. Multi-model mean Hovmöller plots of percentage AMOC weakening for (a) depth-space and (b) density-space over the historical (1905-2014) and ssp585 (2015-2095) experiments, relative to the historical reference period (1850-1899). AMOC weakening is taken as a rolling decadal average. Threshold lines of 5%, 15%, 25% 35% and 45% weakening are shown.

latitudes broadly overlap the OSNAP latitudes. Depth-space performs better for early warning when measured at the latitude of most intense weakening (∼ 45°N) to 26°N. For 25% weakening, depth-space weakening at 45°N precedes 26°N by 9 years for ssp585 (ranging over 9-15 years, depending on scenario). Density-space still generally outperforms along this latitude range, with a time difference of 11 years for 25% weakening in ssp585 (ranging over 11-16 years, depending on scenario) and still has the additional signal from further north (8 years for 25% weakening in ssp585). For less than 10% weakening, depth-space signal precedes the density-space signal by 0-7 years. This is likely due to the high latitude (40-60°N) weakening between 2000-2015 that is seen in depth-space and not density-space.

The timescales for the southward propagation of AMOC weakening are longer than the propagation of density anomalies (e.g. Zhang (2010); Hodson and Sutton (2012)), however they do align with timescale of some studies on AMOC adjustment to high latitude forcing (Kwon and Frankignoul, 2014; Gerdes and Köberle, 1995; Döscher et al., 1994). This will be discussed further in Sect. 4.

The gradient of threshold lines (here-on referred to as "weakening gradients") can be taken as a proxy for the propagation speed of weakening through the basin. The weakening gradients are calculated for each model and each scenario and are calculated in the unit degrees per year (deg yr^{-1}). There are two approaches for considering the MMM weakening gradients.

Method 1: Calculating weakening gradients of the MMM Hovmöller threshold lines (seen on Fig. 3). We call this the explicit multi-model mean (EMMM) (Figs. 4a and 4b, solid black line).

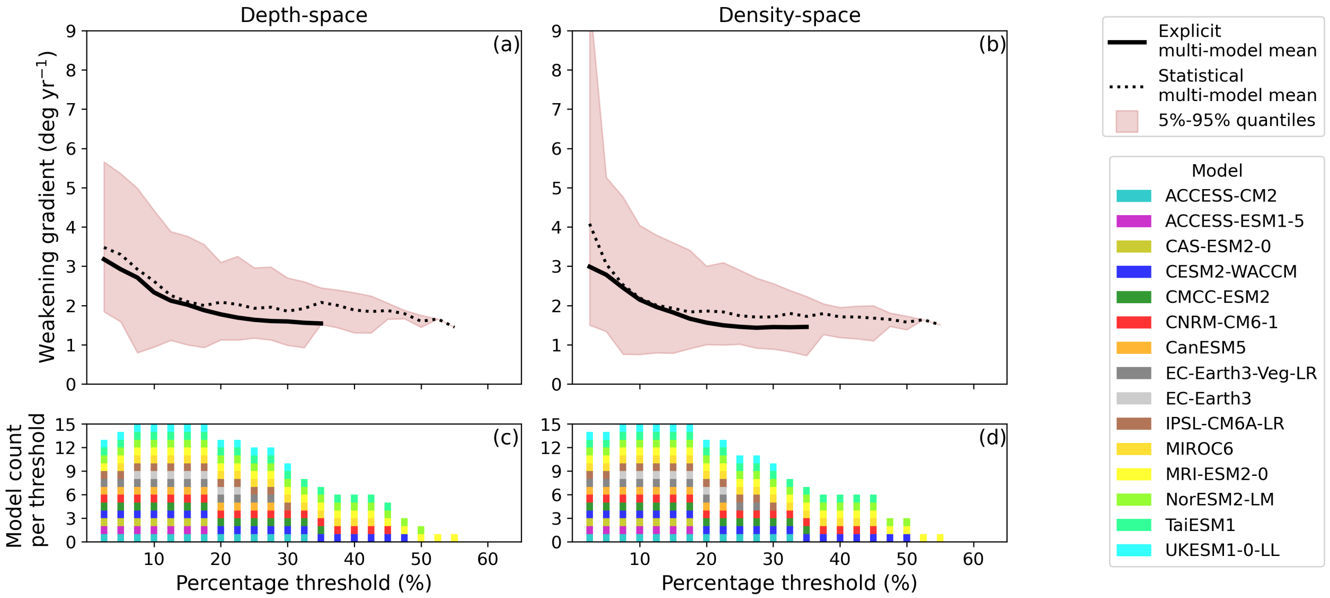

Figure 4. The weakening gradient of the threshold lines (between 40°N and 30°N) at 2.5% intervals for (a) depth-space and (b) density-space. The continuous black line are the weakening gradients of multi-model mean threshold lines, as seen in Figure 3. The dotted black line is the statistical multi-model mean, calculated from the individual weakening gradients of the model set, and the red shading is the 5%-95% quantile range of the model set. (c,d) The models included for the statistical calculations at each threshold. The speed of the weakening gradient is measured in degrees per year.

Method 2: At each threshold, computing the weakening gradient of each model individually before taking the mean across all the models. This does not include the MMM Hovmöller threshold lines. We call this the statistical multi-model mean (SMMM) (Figs. 4a and 4b, dotted black line).

All the models in the model set contribute to all the values of the EMMM weakening gradients whereas since the SMMM weakening gradients are calculated separately at each threshold, the number of models involved can vary (Figs. 4c, 4d). Analysis will primarily focus on the EMMM weakening gradients with the SMMM weakening gradients and associated 5%-95% quantiles acting as a reference for the behaviour of the model set.

For both depth-space and density-space, there is a gradual decline of the EMMM weakening gradient ending in a plateau starting at around the 25% threshold as the threshold increases. The EMMM weakening gradient slows from 3.18 deg yr^{-1} to 1.54 deg yr^{-1} for depth-space and 2.99 deg yr^{-1} to 1.46 deg yr^{-1} for density-space, i.e. in both representations propagation speed of AMOC weakening has halved. The story is similar for the SMMM weakening gradient, although the gradients are consistently slightly higher (by an average of 0.28 deg yr^{-1}) and due to a handful of models with weakening gradients at high thresholds, the SMMM weakening gradients persist along higher thresholds. The SMMM weakening gradients at high threshold should be considered cautiously, since the number of models contributing to statistical calculations are diminishing (Figs. 4c, 4d).

The interpretation of Fig. 4 is that as the AMOC weakens there is a gradual slowdown in the southward speed of propagation of AMOC weakening, down to a minimum propagation speed. This is consistent in both depth and density space analysis. The only difference in the 5%-95% quantiles between the two representations is an anomalous spike at the 2.5% threshold in density-space (Fig. 4b) and this is due to an issue with the MIROC6 weakening gradient at this threshold. Further discussion on individual model behaviour follows in Sect. 3.3.

Figure 4 shows an intriguing slowdown of propagation speed of a weakening signal as the AMOC weakens but also poses three questions: 1) Do all future projection scenarios have similar weakening gradients? For example, does a 25% reduction in the AMOC propagate at the same speed across the Atlantic basin regardless of specific forcing? 2) Do individual models follow the same gradient curve as the EMMM? 3) Why does the gradient slow at lower thresholds and plateau at higher thresholds?

The next section (Sect. 3.2) will address the first question and Sect. 3.3 will address the second question while the third question will be a topic of discussion.

The differences between depth and density-space have been explored in this section. While there are differences between the high latitude response to AMOC weakening in depth-space and density-space, the behaviour in propagation speed south of 40°N is comparable between the two representations. As density-space reveals more details of high latitude processes than depth-space and is more descriptive for AMOC propagation in connection to those high latitudes (Zhang, 2010; Kwon and Frankignoul, 2014), the remainder of the analysis will be presented using the density-space representation. This will capture a more complete representation of weakening than depth-space will. There is very little difference between depth and density space and the equivalent figures for depth-space have been included in the supplementary materials.

3.2 The ScenarioMIP experiments

This section explores differences in density-space AMOC weakening between the future scenarios; ssp126, ssp245, ssp370 and ssp585.

To initially assess differences between scenarios, timeseries of AMOC weakening are shown for 3 selected latitudes of 51°N, 26°N and 30°S (Fig. 5). As was inferred from Fig. 3, the rate of AMOC weakening is greatest at high latitudes (51°N) and is slower at lower latitudes (26°N and 30°S). The latitude with the greatest divergence in AMOC weakening between scenarios is 51°N with end of century MMM weakening of 63% in ssp585 and 41% in ssp126 but also the largest standard deviations for those two experiments of the latitudes (Fig. 5a). Contrasted with weakening of 47% in ssp585 and 32% in ssp126 at 26°N (Fig. 5b) and 25% in ssp585 and 22% in ssp126 for 30°S (Fig. 5c), it indicates weakening of the AMOC in northern latitudes are more responsive to climate forcing than further south. This can also be seen in Fig. 5c, as the AMOC at 30°S begins the 21st century with elevated strength compared to the reference (10% greater) and takes until the mid 2030s (depending on scenario) to exceed 0% weakening while the two higher latitudes start weakening by 2015. The divergence between scenarios appears mainly driven by a slowdown of weakening in the lower emissions scenarios (ssp126 and ssp245) as the rate of weakening for ssp370 and ssp585 appears largely unchanged over each timeseries. A point of interest is that the AMOC weakening for ssp370 is consistently less than the other three experiments until the mid-2060s, contrary to the expectation that higher emissions scenarios lead to greater AMOC weakening, but by the end of the century the amplitude of

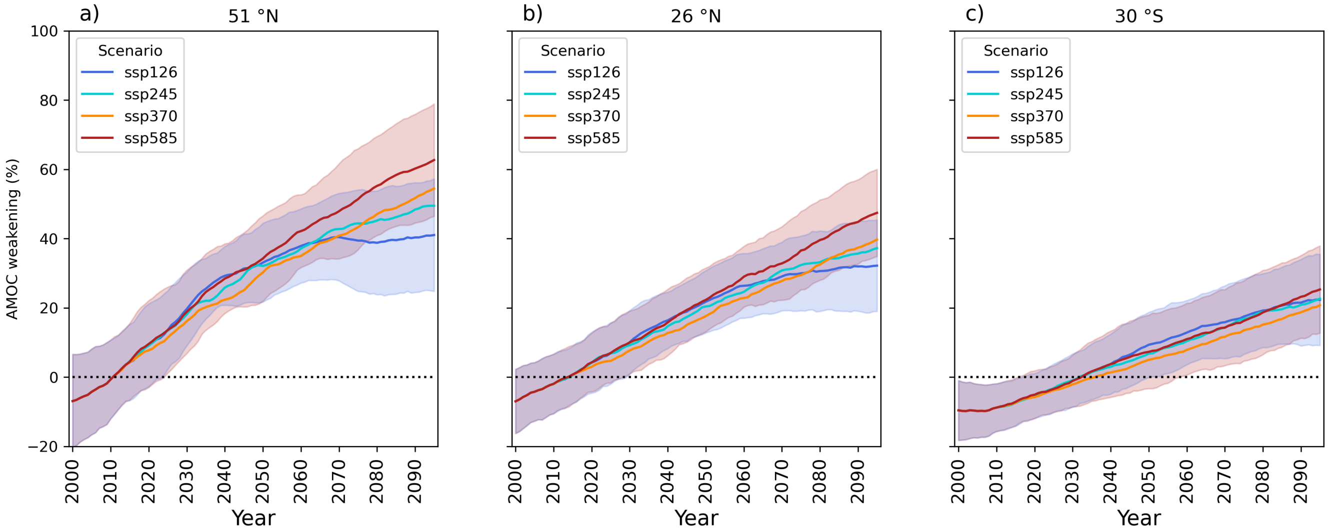

Figure 5. Timeseries of MMM AMOC weakening for the four scenarios relative to the 1850-1899 reference at (a) 51°N, (b) 26°N and (c) 30°S. Red and blue shading show 1 standard deviation for ssp585 and ssp126, respectively.

weakening in each scenario corresponds to the severity of the emissions in that scenario. Another point of interest with ssp370 is that it has a slower rate of decline to the other scenarios prior to 2050, in disagreement with what was found by Weijer et al. (2020). This may be due to differences in the method of calculating the timeseries, such as this use of percentage difference taking the rolling decadal average rather than rolling annual average, or because our study uses a smaller number of ensemble members than their study used.

Relative to the 1850-1899 reference period, the AMOC is shown to already be in decline from the year 2000 at 51°N (Fig. 5a) and 26°N (Fig. 5b), which is model dependent and due to the model's sensitivity to aerosols (Robson et al., 2022). While the RAPID array has not yet detected significant decline across 2004-2022 (Jackson et al., 2022), statistically significant decline has been seen in specific water masses after decomposing the AMOC (e.g. in the deep western boundary) (Pita et al., 2025). Observational arrays are subject to large internal variability which could obscure AMOC decline. Longer timescales of observations are required to detect any decline of the real-world AMOC, with Lobelle et al. (2020) proposing at least 29–67 years of RAPID observations to be at the 90% confidence level of detection, but decomposing the AMOC as was done by Pita et al. (2025) could reduce this timescale. Decline has not yet been significantly observed by OSNAP (2014-2021) (Li et al., 2021).

Having assessed AMOC decline at specific latitudes, we now consider the full basin response to AMOC weakening for the four scenarios. All scenarios exhibit a north-to-south propagation of weakening (Fig. 6) with weakening onset at high latitudes similar to what was shown for ssp585 in Sect. 3.1. At a glance, Hovmöller plots are broadly similar for the first 50 years with similar threshold lines of 5% and 15% weakening after which the scenarios start diverging with ssp585 experiencing the

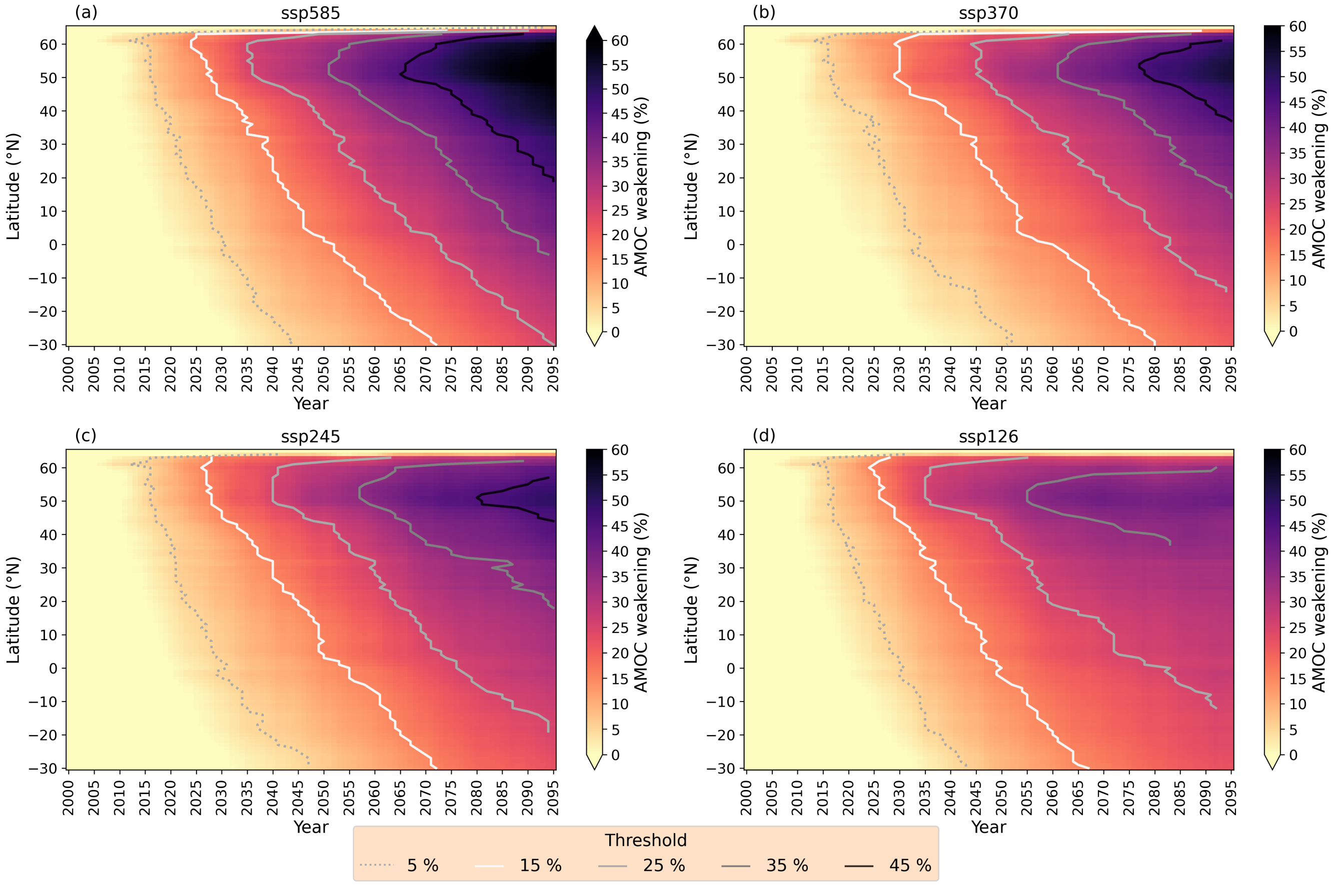

Figure 6. Multi-model mean weakening Hovmöller plots for the four ScenarioMIP scenarios (2000-2095) in density-space. Scenarios are (a) ssp585, (b) ssp370, (c) ssp245, (d) ssp126. Threshold lines of 5%, 15%, 25%, 35% and 45% are shown where they exist. (a) is as seen in Figure 3b, but the colourmap here is different to explicitly highlight weakening.

greatest weakening and ssp126 experiencing the least. Detailed comparisons between scenarios are found by taking pairwise differences of the four Hovmöller plots, testing for 95% significance of difference found with a student t-test (Fig. 7).

Considering the scenarios compared to ssp585, the greatest magnitude end of century differences are with ssp126 (Fig. 7a), with smaller differences for ssp245 (Fig. 7b) and smaller again for ssp370 (Fig. 7c), consistent with Fig. 5. Interestingly, there are hardly any significant differences between ssp585 and either ssp126 or ssp245 before 2050. When the differences do become significant they do not propagate at the speed of the weakening gradients but can occur over a large range of latitudes in a single year and at least for the case with ssp245, it appears the equator may present a barrier for differences to propagate across (Fig. 7b). This is not seen in Fig. 7c, as the ssp370 and ssp585 are significantly different for the vast majority of the basin and time period because at every latitude AMOC weakening for ssp370 is less rapid than for ssp585 (Fig. 5).

The remaining pairwise differences emissions scenarios (ssp126, ssp245 and ssp370) are characterised by less extreme emissions scenarios experiencing greater weakening than the more extreme emissions scenarios, especially before 2070 (Figs. 7d-f). This is contrary to what we expect from the end of the century, and indeed after 2070 this trend is reversed, especially north of 50°N. In comparisons with ssp370, significant differences south of the equator persist until the 2090s. Comparing similar experiments (ssp370 and ssp245, Fig. 7e) and (ssp245 and ssp126, Fig. 7f), there are wavelike periods with no significant differences in AMOC weakening possibly driven by multi-decadal variability aligning AMOC strengths. Figures 7d and 7f also show an indication that the equator is a barrier for differences to cross.

The ssp370 scenario has been shown to be consistently different from the other scenarios (Figs. 7c-e) and with a different rate of decline of weakening (Fig. 5). This scenario is characterised by high aerosol emissions, which have been linked with strengthening the AMOC (Menary et al., 2020). The increased presence of aerosols in the atmosphere may explain the slower decline of the AMOC in this scenario.

Figure 7 explores the magnitude and spatial distribution of differences in AMOC weakening between scenarios but to understand differences in latitudinal connectivity we must return to Fig. 6. At high threshold ($\geq 25\%$) the threshold lines in the lower emissions scenarios reduce in gradient, southward propagation is slower, while in higher emissions scenarios there isn't such a noticeable change in the threshold line gradient (Fig. 6). The reduction in weakening gradient for lower emissions scenarios is clear in Fig. 8 as is the relatively constant propagation speed in the high emissions scenarios. In Fig. 8, both ssp126 and ssp245 show a continuous decline in weakening gradient as threshold increases while for ssp370 and ssp585 the weakening gradient initially declines but plateaus at high thresholds. The EMMM weakening gradient for ssp370 also starts lower than any of the other experiments with the 2.5% threshold gradient at 2.50 deg yr^{-1} compared to 2.99 deg yr^{-1} (ssp585), 2.92 deg yr^{-1} (ssp245) and 3.04 deg yr^{-1} (ssp126), further supporting its uniqueness from the other experiments.

The plateau of high threshold weakening gradient could indicate a minimum speed of propagation in response to strong forcing that is not required for weaker forcing. Alternatively, depending on what the mechanism for southward propagation of weakening is, if the driver of weakening stops or slows in lower emissions scenarios, it is plausible that the southward progression of a weakening signal would stop or slow as well. Figure 5 shows that the rate of AMOC decline varies as a function of latitude. The process that sets the rate of decline at a fixed latitude is not the object of this study but we posit is strongly related to the propagation of AMOC anomalies through the basin. Exactly understanding the mechanism that propagates weakening southward would provide insight into this slowdown across the scenarios. Does weakening in the high latitudes and SPG necessitate weakening for the rest of the AMOC?

Figures 8c and 8d show a divergence between the multi-model mean line and the statistical multi-model mean line, where the statistical multi-model mean plateaus rather than continuously declining. This is a surprise, but considering the number of models involved in the high threshold statistics (Fig. 8e-h), this divergence only occurs between the multi-model mean and a small number of models. As will be shown in Sect. 3.3, most models show similar behaviour to the multi-model mean rather than the statistical model mean.

https://doi.org/10.5194/egusphere-2026-575
Preprint. Discussion started: 11 February 2026

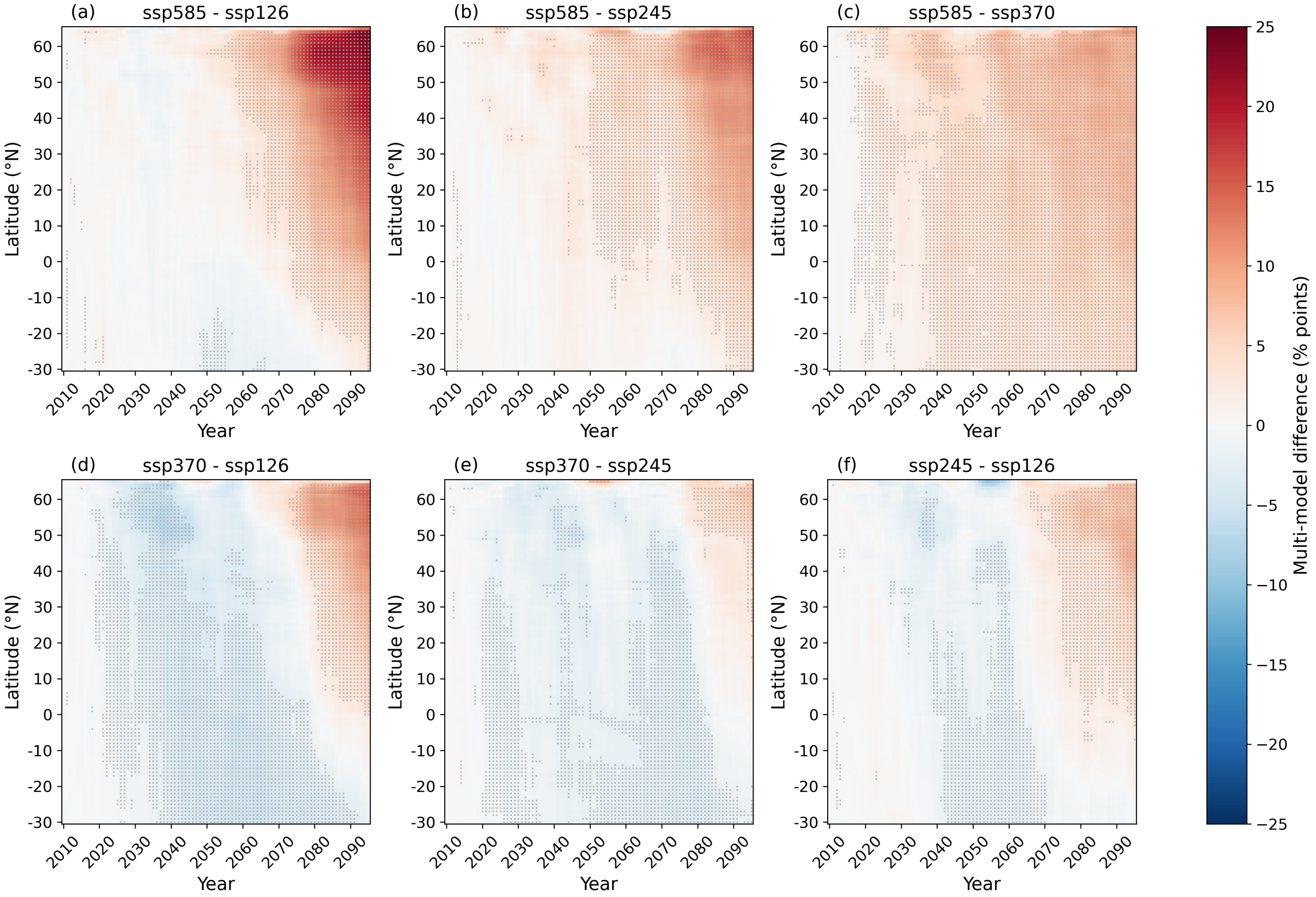

Figure 7. The pairwise differences AMOC weakening between the four ScenarioMIP experiments. Weakening in the more extreme emissions scenario is subtracted by weakening in the less extreme emissions scenario. Positive (red) means the more extreme emissions scenario has greater weakening, negative (blue) means the less extreme emissions scenario has greater weakening. 95% significance from a student t-test is indicated by a dot.

3.3 Inter-model comparison

Until this point, the MMM behaviour has been the focus of this study. However, it is not expected that all models will behave in a consistent manner, as suggested by Fig. 8e-h. Therefore, this section will focus on comparing the differences in southward propagation across the CMIP6 models included in this study. These models are shown for scenario ssp585 and ssp126 at the two extremes of future forcing. Scenario ssp370 has been repeatedly mentioned in this paper for deviating from the other scenarios but it is more informative for comparing individual models to study the two extremes (ssp126 and ssp585).

Models are categorised according to their ssp585 weakening gradients. For each model, the 1st (2.5%), (N/2)th and Nth weakening gradients are taken, where N is the model's maximum gradient. Splitting the thresholds into two groups allows for

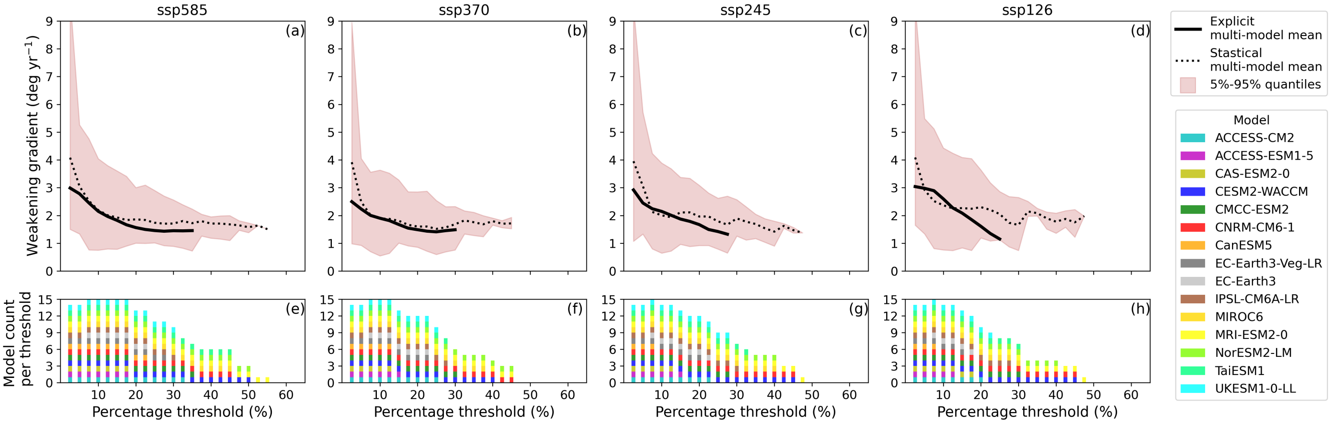

Figure 8. Density-space weakening gradients, as seen for ssp585 in Fig. 4, for all four ScenarioMIP experiments. (a) ssp585, (b) ssp370, (c) ssp245, (d) ssp126 and (e-h) the models used for the statistical multi-model mean and shading.

comparing if the weakening gradients behaviour changes from low to high threshold. Differences between the 1st and (N/2)th gradients and the (N/2)th and Nth gradients are found. Small differences ($< |0.5|$) imply the gradients are fairly constant with threshold while large differences ($> |0.5|$) imply the gradients are changing with threshold. The UKESM1-0-LL first difference is -0.20 deg yr^{-1} and its second difference is -0.20 deg yr^{-1} (Fig. 9f), which is defined as a 'constant' gradient. While the UKESM1-0-LL weakening gradient does reduce by 0.40, it is far more constant than the changes seen in NorESM2-LM or TaiESM1. The NorESM2-LM first difference is -3.47 deg yr^{-1} and its second difference is -1.57 deg yr^{-1} (Fig. 9h), putting it in the 'continuous decline' group. Meanwhile, the first difference for TaiESM1 is -3.30 deg yr^{-1} and its second difference is -0.10 deg yr^{-1} (Fig. 9i), putting it in the 'decline to plateau' group, which can be seen in Fig. 9i as the gradient has declined from 5.34 deg yr^{-1} to a relatively constant gradient of ~ 2.0 deg yr^{-1} (with some variation). A complete breakdown of the categorisation by model is shown in Table 2 and explored further in Appendix A, with the first and second differences shown by Fig. A1.

The two further categories are declining to increasing gradient (e.g. Fig. 9j) and inconclusive gradients (not shown here). The EMMM gradient behaviour is a decline to plateau. The inconclusive models include those that have a limited number of thresholds to categorise (ACCESS-ESM1-5, CAS-ESM2-0, EC-Earth3) and have erroneous linear fits (MIROC6).

The sub-set of models chosen to illustrate the differences in weakening gradient behaviour between models are IPSL-CM6A-LR, MRI-ESM2-0, NorESM2-LM, TaiESM1 and UKESM1-0-LL. The weakening Hovmöllers for these models under ssp585 forcing are shown in Figs. 9a-e and the weakening gradients are shown in Figs. 9f-j. These selected models skew towards greater AMOC weakening than the rest of the models. This is in part because models with higher percentage weakening have more threshold lines, which is ideal for illustrating the differences in model response. The choice to include two constant gradient models (MRI-ESM2-0 and UKESM1-0-LL) was made to highlight differences in weakening between ssp126 and ssp585 and will be commented upon later.

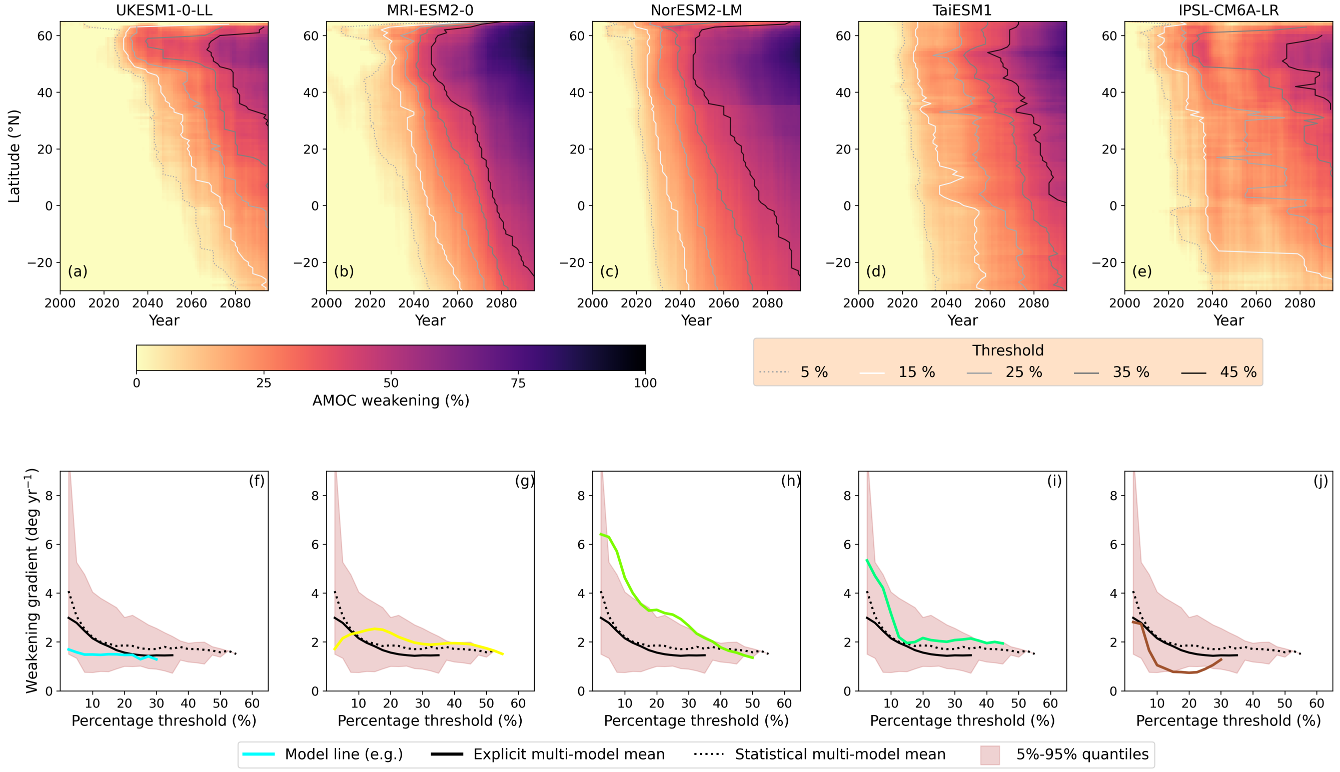

Figure 9. AMOC weakening in density-space for a model subset for ssp585. (a-e) Individual model Hovmöller plots shown with threshold lines of 5%, 15%, 25%, 35% and 45% reduction. (f-j) Individual weakening gradient plots imposed over the multi-model mean gradient and statistics. Hovmöller and weakening gradient plots of the full model set can be found in Appendix B.

Constant Gradient	Continuous Decline	Decline to Plateau	Decline to Increase	Inconclusive
CanESM5	CMCC-ESM2	CESM2-WACCM	ACCESS-CM2	ACCESS-ESM1-5
MRI-ESM2-0	CNRM-CM6-1	EC-Earth3-Veg-LR	**IPSL-CM6A-LR**	CAS-ESM2-0
UKESM1-0-LL	**NorESM2-LM**	**TaiESM1**		EC-Earth3
		The EMMM		MIROC6

Table 2. CMIP6 models sorted according to their weakening gradients in response to ssp585 forcing. Constant gradient indicates a similar gradient regardless of threshold. Continuously declining means as threshold increases the gradient noticeably decreases. Declining to plateau indicates an initial decrease in gradient that plateaus at a constant gradient. Declining to increasing means the gradient reduces and increases again. Inconclusive are model with insufficient (less than a 20% range) of thresholds to analyse or MIROC6, with low confidence in some of the linear fits. Models in bold are in the model subset.

The models with the largest initial weakening gradients are the ones that show the greatest decline. NorESM2-LM and TaiESM1 have fast weakening gradients for the 2.5% threshold line (6.41 deg yr^{-1} for NorESM2-LM and 5.34 deg yr^{-1} for TaiESM1) but where the NorESM2-LM propagation speed slowly declines as the threshold increases (to a minimum of 1.34 deg yr^{-1}), TaiESM1 propagation speed reduces rapidly until 15% weakening and subsequently plateaus at a mean value of 2.04 deg yr^{-1}. The models with constant gradient propagate at a slower speed for all thresholds (MRI-ESM2-0, with a mean speed of 2.08 deg yr^{-1} and UKESM1-0-LL with a mean speed of 1.68 deg yr^{-1}), closer to the speed TaiESM1 plateaus to. The slower propagation speed of weakening in UKESM1-0-LL is noticeable when considering the 5% threshold line in Fig. 9a, with the signal taking 42 years to propagate from 40°N to 30°S.

Changes to the AMOC in the SPG region is more nuanced in the individual model cases than in the MMM. IPSL-CM6A-LR and UKESM1-0-LL experience substantial reductions in the SPG region (49°N to 63°N) that are not immediately propagated southwards, most noticeable in the 35% threshold line (Figs. 9a and 9e). This could indicate high latitude decline in the streamfunction may not immediately propagate further south. A recent high resolution modelling study (Petit et al., 2025) found that there is a strong relationship between AMOC density at OSNAP latitudes with AMOC strength at 45°N but not between AMOC strength at OSNAP latitudes (53-60°N) and 45°N, which adds credibility to this lack of immediate propagation. The other three models show much broader weakening over the SPG region (Figs. 9b-d) and display greater connectivity between the high and lower latitudes. These models do seem in disagreement with the results from Petit et al. (2025), but given the differences in experimental set-up and model resolutions, it is difficult to assess whether the disagreement has any significance. NorESM2-LM does show a break in weakening at 35°N which aligns with Zhang (2010)'s different proposed propagation regimes north and south of Cape Hatteras, but other models do not show this break.

An increase in weakening gradient as threshold increases, as seen with IPSL-CM6A-LR (Fig. 9j), is not inherently physically implausible. However, when taken in consideration of the Hovmöller plot (Fig. 9e), it appears more likely to be a limitation of the threshold line method than a physical process. While the method is good at capturing the behaviour of coherent decline (e.g Figs. 9b and 9c, or the multi-model mean seen in Fig. 6), the threshold lines become incredibly noisy when presented with internal variability, whether that is from multi-decadal variability or other oscillatory behaviour in AMOC strengthening and weakening, such as the band of relative strengthening seen between 2040-2050 in Fig. 9e. It then becomes questionable whether the gradients of these lines truly represent the propagation speed of AMOC weakening — to what extent does internal variability become a part of the signal that is propagating? Furthermore, assuming the weakening to strengthening seen in the 2030-2050 period is due to internal variability, it is difficult to say if the variability is suppressing what would have been a 35% weakened state after 2040 or if the variability had enhanced the weakening to 35% prior to 2040 and the reduction in strength is a return to the normal. This is something that could be addressed with investigating multiple ensemble members of the various models, which is beyond the scope of this study. As such, while two models (ACCESS-CM2 and IPSL-CM6A-LR) have been identified to have increasing weakening gradients, this categorisation may be more the result of internal variability and limitation of the methodology than an increase in physical propagation speed.

Figure 10 shows the same models as in Fig. 9 but under ssp126 forcing. All models, with the exception of MRI-ESM2-0, show fewer and less steep (e.g. slower) threshold lines in the ssp126 experiment. This is confirmed when looking at the weakening gradients (Figs. 10f-j), where all except MRI-ESM2-0 show a decline in gradient with increased threshold similar to the multi-model mean. MRI-ESM2-0 experiences similar weakening and weakening gradients between ssp126 and ssp585. An interpretation of this is that for MRI-ESM2-0, the severity of AMOC weakening is largely resultant from the historical forcing and associated feedbacks. Linking this with a comment made in Sect. 3.2, the SMMM weakening gradients at high percentage threshold of ssp126 is skewed by the behaviour of MRI-ESM2-0 and CNRM-CM6-1 and the EMMM weakening gradient is more consistent with most models (see Appendix B, Fig. B4).

The reduction in weakening gradient appears to be due to a strengthening of the AMOC in ssp126 in the last two decades cutting off the 45% threshold line in Fig. 10c and the 35% line in Figs. 10d and 10e. However as previously discussed regarding IPSL-CM6A-LR in ssp585, it is not clear if this strengthening is due to a genuine strengthening due to different external forcing or is a mode of internal variability within the system. As is seen with MRI-ESM2-0 (Fig. 10b), it is possible for weakening signals to propagate under ssp126 forcing similarly to how they do under ssp585 forcing (Fig. 9b).

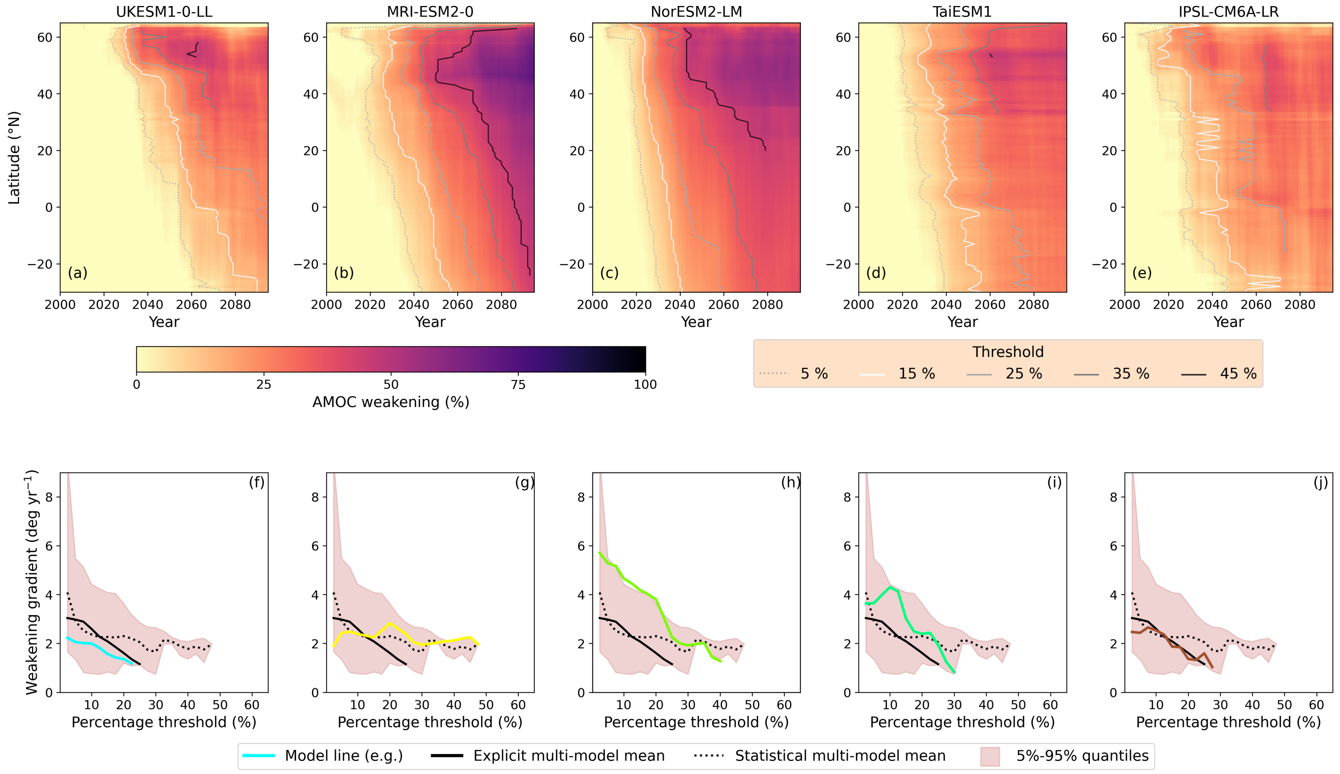

Figure 10. The same as Fig. 9 but for ssp126.

No relationship was found between either propagation speed or propagation categorisation and the mean AMOC strength.

4 Discussion

This study has explored AMOC weakening as a function of time and latitude in the four CMIP6 future scenarios. The analysis has shown a north-to-south propagation of AMOC weakening, led by weakening in the subpolar North Atlantic (Fig. 3), with variation to the speed and extent of southward propagation dependant on future forcing and the threshold of weakening (Fig. 6 and 8). Reduction in southward propagation of weakening is both scenario and model dependent; for the MMM in high emissions scenarios (ssp585, ssp370) the propagation speed reduces then plateaus at higher thresholds ($> 20\%$) while for low emissions scenarios (ssp245, ssp126) it declines continuously. An interpretation of these results is that there could be two mechanisms at play, a low threshold/low forcing declining signal in the propagation speed seen in ssp245 and ssp126 and a high threshold/high forcing constant propagation speed which the AMOC transitions to. Additionally, weakening in the lower emissions scenarios is more locally constrained to the North Atlantic. It is unclear if the slowdown of the propagation speed is the cause or the result of this local constraint.

There are broad similarities with propagation speeds and the magnitude of AMOC weakening in depth-space and density-space south of 40°N, which is expected given the similarities of the streamfunctions at these latitudes (Kwon and Frankignoul, 2014). Crucially, north of 40°N the density-space streamfunction reveals a higher latitude origin of the weakening signal for each given threshold and as seen in Fig. 3 weakening is detected sooner in density-space than depth-space. As such when considering latitudinal connectivity AMOC decline the use of density-space is likely more informative than depth-space (in agreement with Zhang (2010)).

In the inter-model comparison, it was further found that for individual models while AMOC weakening often is first onset in the SPG, it does not always immediately translate to AMOC weakening further downstream (Fig. 9). This is particularly true for AMOC weakening in lower emissions scenarios (Fig. 10). The strength of the SPG has been shown to increase in some models even as the AMOC declines (see Fig 8 in Dong et al. (2025)) and the relationship between the SPG strength and the AMOC is an active area of research.

Changes to the mixed layer depth (MLD) at sites of deep convection have not been considered in this study but are vitally important for understanding the changes to the AMOC. Comparing results and supplementary material from a recent study on AMOC collapse by Drijfhout et al. (2025) with our results, there are no obvious connections between the changes in MLD they found and the propagation speeds we found. Considering three models that are in both studies and have been identified here as having a constant propagation speed of weakening under ssp585 forcing (MRI-ESM2-0, UKESM1-0-LL and CanESM5), neither the spatial extent of the convective regions nor the rate of MLD change appear similar enough to suggest an obvious connection between these and the changes to the propagation speeds we observe.

Understanding the relationship between scenario forcing, AMOC weakening and AMOC connectivity is important for improving predictions for future AMOC decline. The other key revelation regarding future scenarios is that for ssp370 (characterised by greater atmospheric aerosols relative to the other scenarios), the rate of AMOC decline is slower than the other scenarios (Figs. 5 and 7), contrary to the findings of Weijer et al. (2020). It's possible this disagreement could be related to the specific models chosen to study or the differences in methodology. Menary et al. (2020) showed aerosol forcing in CMIP6 strengthens the AMOC and we propose the increased aerosol content in ssp370 is what slows the decline. The same study showed that the response to aerosols may be overstated compared to reality so our results may be more pronounced than observations would show.

The threshold weakening gradients for the model set shows a wide range of behaviour, categorised in Table 2. The categories provide an avenue for understanding model spread with some models showing a constant propagation speed with AMOC decline and other models showing a decline in propagation speed with AMOC decline. There is no obvious connection between propagation speed and the historical mean state AMOC. While this study has not gone into detail on the mechanics behind AMOC weakening or propagation, it is clear that the speed of weakening occurs on a slower timescale than the speed of density anomaly propagation in the deep western boundary current (Zhang, 2010; Kostov et al., 2022). Thus, AMOC weakening is likely either facilitated by the slow advection of anomalies (Gerdes and Köberle, 1995; Zhao et al., 2017) as has been somewhat illustrated in a 1 degree resolution simulation by Weijer et al. (2012) or is facilitated by the decadal adjustment of thermal wind balance in response to high latitude forcing (Döscher et al., 1994; Marshall and Johnson, 2013; Ortega et al., 2021). Given all the models in this study are non-eddying, with a nominal horizontal resolution of 1°, the real world applicability of these results may be limited and the propagation speed of AMOC weakening may be faster than shown here due to better resolved eddy processes (Hodson and Sutton, 2012; Weijer et al., 2012). Increasing the number of high resolution models running the future scenario experiments and outputting the necessary variables to analyse the AMOC streamfunction would be essential to address the effect of resolution on propagation speed. Whether the differences seen in weakening gradient behaviours indicate different mechanisms of AMOC weakening propagation in the ensemble of 1-degree resolution CMIP6 models requires further work.

There are a few limitations with the threshold line method. The main weaknesses to the method are for implementation on models that exhibit high degrees of internal variability or non-smooth decline. The impact of variability is partly resolved with the decadal smoothing applied, however there are still models that still exhibit noticeable variability. For these models (e.g. IPSL-CM6A-LR) the threshold lines become increasingly noisy especially as the signal of internal variability spans the basin faster than the signal of weakening. Appendix D contains timeseries of relative AMOC strength at 51°N (Fig. D1) and 26°N (Fig. D2) which gives an sense of internal multi-decadal variability. The confidence in the gradient calculation of such threshold lines is then reduced and there is the question to how representative the threshold gradient is of the propagation of a weakening AMOC. Internal variability could be less of an impact when considering multiple ensemble members of a single model. CanESM5, for example, has a large number of ensembles. Unfortunately, most modelling centres only use a handful of ensemble members (if they simulate more than 1) for the experiments used in this study. Additionally, the necessary variables from those simulations to calculate the density-space streamfunction are not always available. It is therefore not achievable to disentangle the weakening signal from the internal variability for all models.

Another limitation of the threshold method is the requirement for a reference AMOC to compare AMOC weakening against. The chosen reference period cannot be too close to the start of the time period of interest (2015-2100), otherwise one might not capture the true onset of a weakening signal and threshold line, and weakening gradients represent a deviation from the reference rather than a propagation signal. This was found to be the case when using a reference of 1995-2014 (not shown).

The reference period chosen was 1850-1899, however this has its own uncertainties associated with a sparsity of measurements from this time (Robson et al., 2022). However, these two issues of internal variability and uncertainty in the historical reference are by no means unique to this study.

Further limitations might arise by not clearly establishing the start of the weakening. For instance, the anomalously large weakening gradient of 2.5% for MIROC6 could be the result of starting the analysis period (2000-2095), when the AMOC had already weakened relative to the reference. CMCC-ESM2 and EC-Earth3 also have relative strength less than 100% in the year 2000. CMCC-ESM2 appears to have started declining before the other models whereas EC-Earth3 appears to still be strengthening until 2020, possibly due to internal variability (see Appendix D). Thus, future analysis into AMOC decline could benefit from defining the period of decline for each model from the point of a maximum AMOC strength rather than defining change within a fixed prescribed time window for all models.

5 Conclusions

This study addresses the varied latitudinal response across CMIP6 models and future scenarios. It has highlighted the spread in propagation speed of AMOC weakening in the CMIP6 model ensemble, with some signals propagating over 6 deg yr^{-1} and others less than 1 deg yr^{-1}. We also identified that speed of propagation can slow as the AMOC slows, although this is model and scenario dependent and is likely a combination of changes to ocean circulation as well as changes to the high latitude source of deep water. As this study has not investigated mechanisms, further work is required to disentangle the mechanisms that drive the propagation of AMOC weakening. Through understanding the mechanisms that distribute the weakening signal through the Atlantic, we may better understand why different CMIP6 models project different severities of AMOC weakening particularly when measured at latitudes south of deep convection (e.g. at 26 °N).

The differences between weakening in the depth-space and the density-space representation of the AMOC were investigated. The downstream (south of 40 °N) changes were broadly similar, with similar propagation speeds identified. However, the density-space streamfunction has both its peak strength and latitude of weakening onset further north than the depth-space streamfunction. As such, we suggest when considering latitudinal connectivity and propagation that the density-space representation is more insightful. While the time difference between 45°N and 26°N is comparable for depth-space and density-space (9 and 11 years, respectively, for 25% weakening in ssp585), when considering measurements at latitudes corresponding to OSNAP and RAPID, density-space shows weakening at OSNAP precedes weakening at RAPID by more than a decade than when seen in depth-space (19 years vs 4 years for 25% weakening). This substantial difference is due to the latitude of weakening onset being further south in depth-space.

Additionally, we studied the basin-wide differences between future scenarios and showed that the AMOC weakening for ssp370 is slower than the other scenarios for much of the future period and the initial north to south propagation speed of weakening for the multi-model mean is ~ 0.5 deg yr^{-1} slower than the other scenarios (Fig. 8). We attribute these differences to the aerosol contribution of ssp370 and potentially the over-sensitivity to aerosols in CMIP6 models (Robson et al., 2022).

https://doi.org/10.5194/egusphere-2026-575
Preprint. Discussion started: 11 February 2026

Despite this oversensitivity, ssp370 is a valuable experiment when considering AMOC changes in the first half of the 21st century due to the slower response of weakening than seen in the other ScenarioMIP scenarios.

Improving the understanding of the latitudinal connectivity of AMOC weakening in the subpolar North Atlantic and the rest of the basin could aid the development of early warning signals of AMOC decline with the OSNAP array and the RAPID array (Jackson and Wood, 2020). Understanding the driving mechanism for southward propagation of AMOC weakening and why the weakening gradients behave differently for different models could also provide insight into the CMIP6 model spread. Better understanding of model spread should lead to improved models and improved confidence in predictions of AMOC decline in the 21st century.

Code and data availability. The CMIP6 data used in this study is freely available at https://esgf-node.llnl.gov/search/cmip6/. The code used for this paper is available on request from the lead author.

Appendix A: Model Categorisation

To categorise model behaviours, we compare the differences in the initial, midpoint and final weakening gradient for each model. For example, for UKESM1-0-LL ssp585, the differences are found between the weakening gradients at the 2.5% threshold, the 15% threshold and the 30% threshold. Comparing the first difference (between the initial and midpoint gradients) and the second difference (between the midpoint and final gradients) give an indication of whether a model's weakening gradient is declining, constant or otherwise. It is not a perfectly rigorous methodology but functions to illustrate numerically trends that can be assessed by eye. The model categorisations, based on the ssp585 weakening gradients in density-space (Fig. B3) are shown in Fig. A1. Gradient differences of less than 0.5 degrees per year are considered approximately 'constant', so a first and second difference being constant indicates the gradient is constant. A gradient difference of greater than 0.5 indicates a substantial change in weakening gradient. A large negative first difference and a small second difference indicate declining propagation speed followed by a plateau while having both a large first and second negative difference indicate a continuous decline of propagation speed. A positive difference indicates the propagation speed is increasing with increasing threshold, as can be seen with IPSL-CM6A-LR, ACCESS-CM2 and EC-Earth3. An additional constraint on the categorisation is that models with less than a 20% range of threshold lines in Fig. B3 are considered 'inconclusive' due to a lack of data to comment on trends. These models are ACCESS-ESM1-5, CAS-ESM2-0 and EC-Earth3.

Additionally, the standard deviation of the first group and the second group is found to determine whether the weakening gradients have high variance (> 0.25) or low variance (< 0.25). High variance is found in groups with changing gradient and low variance is found in groups with constant gradients (Fig. A2). The standard deviation plot shows similar groups to the differences plots (Fig A1), indicating that the differences method is accurate at capturing trends in weakening gradient changes despite its simplicity. Categorisation from the differences plot is prioritised over the standard deviation plot as it directly shows

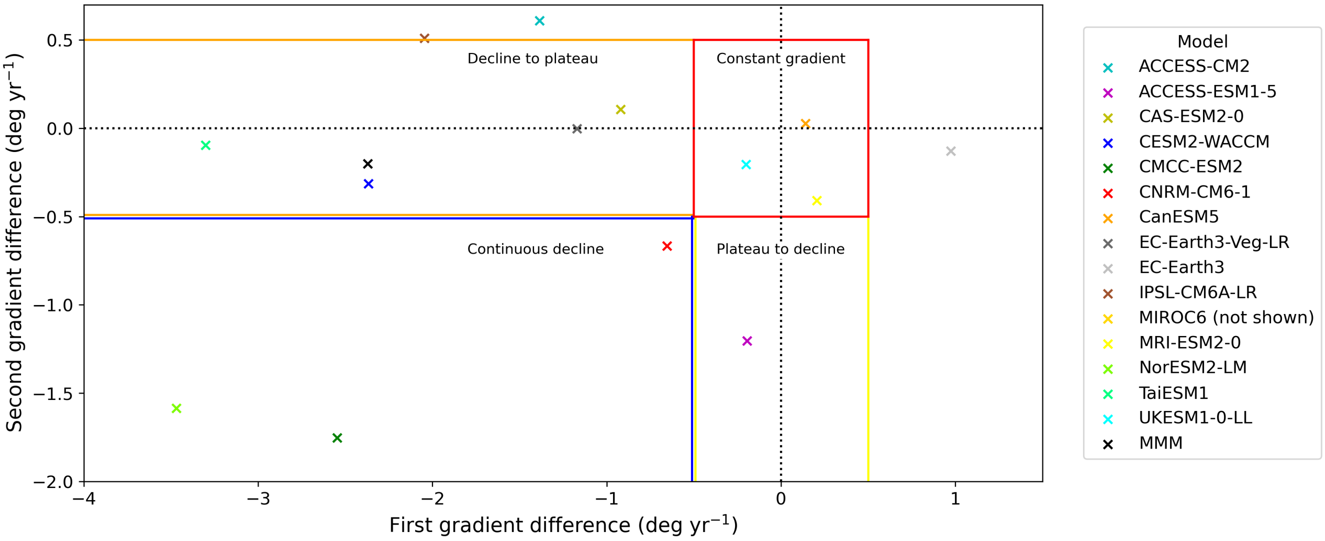

Figure A1. Categorisation of model behaviour in ssp585 density-space weakening, based on differences in weakening gradients. Labels and boxes show key categorisations.

545 an increase or a decrease of weakening gradient which is obscured with standard deviation which only shows the spread in weakening gradients.

Appendix B: Density Model Set

The full model set Hovmöller and weakening gradient plots for density-space.

Appendix C: Depth Model Set

550 The full model set Hovmöller and weakening gradient plots for depth-space.

Appendix D: Fixed Latitude Model Timeseries

Author contributions. HAK and JM conceptualised the project. HAK designed the methodology, performed the investigation and visualised results. JM, RM, SD, MO and ASF supervised the project. HAK prepared the manuscript with contributions from all co-authors.

Competing interests. The authors declare that they have no conflict of interest.

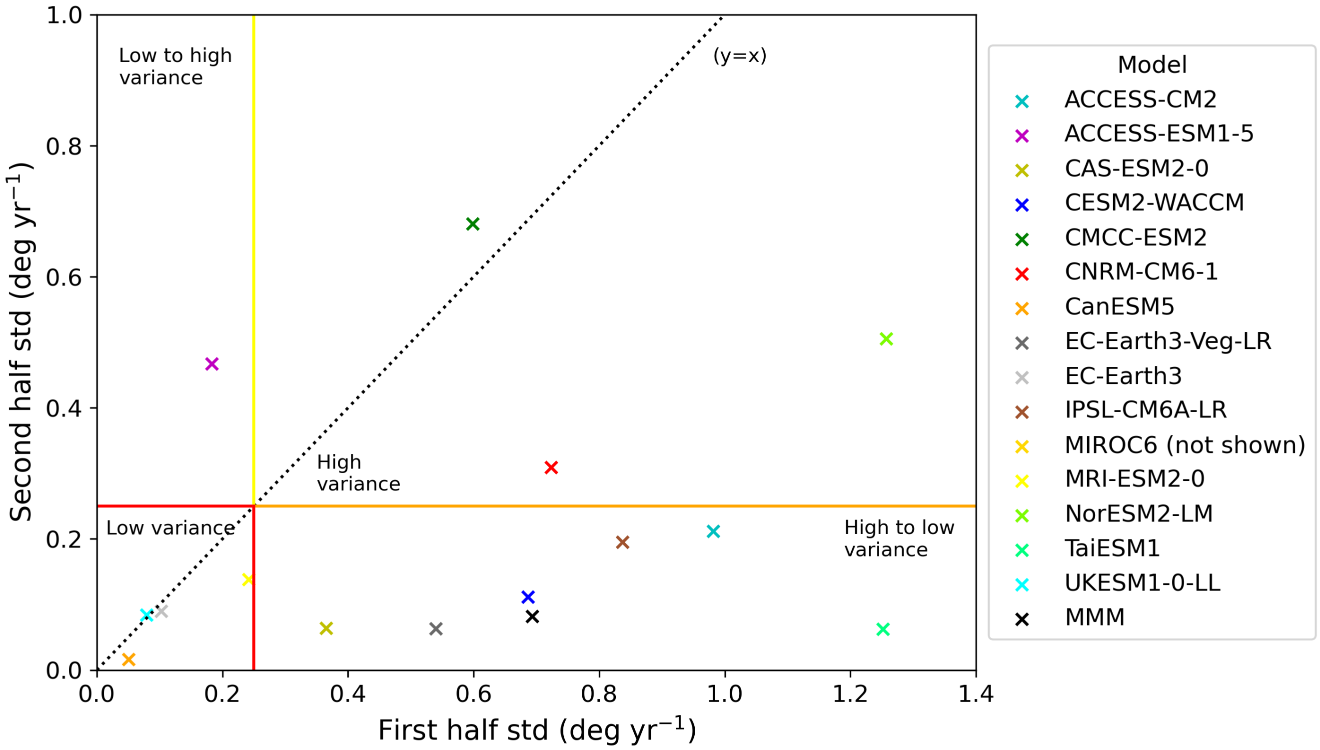

Figure A2. Categorisation of model behaviour in ssp585 density-space weakening into high and low variance groups. These groups broadly agree with the constant gradient, decline to plateau, plateau to decline and continuous decline from Fig. A1. Labels and boxes show groupings.

Acknowledgements. We acknowledge the World Climate Research Programme's Working Group on Coupled Modelling, which is responsible for CMIP, and we thank the climate modelling groups for producing and making available their model output. For CMIP the U.S. Department of Energy's Program for Climate Model Diagnosis and Intercomparison provides coordinating support and led development of software infrastructure in partnership with the Global Organization for Earth System Science Portals. We acknowledge the World Climate Research Programme, which, through its Working Group on Coupled Modelling, coordinated and promoted CMIP6. We thank the climate modelling groups for producing and making available their model output, the Earth System Grid Federation (ESGF) for archiving the data and providing access, and the multiple funding agencies who support CMIP6 and ESGF. The CMIP6 data was accessed and analysed using the UK super-data-cluster JASMIN. HAK received funding from the INSPIRE Doctoral Training Programme, funded by the National Environmental Research Council, UK, under Grant Number: NE/S007210/1. SD and JM received funding from ISOTIPIC (Interacting ice Sheet and Ocean Tipping - Indicators, Processes, Impacts and Challenges), funded by the National Environmental Research Council, UK, under Grant Number: NE/Y503320/1. MO received funding from DIMSUM (Drivers and Impacts of North Atlantic Heat and Freshwater Fluxes), funded by the National Environmental Research Council, UK, under Grant Number: NE/Y005090/1. JM, SD and ASF received funding from SORTED (Subpolar Gyre Observations, models and AI to Resolve Tipping points and provide Early warning Detection) with SCOP Grant Number: SCOP-PR01-P020. MO and JM received funding from CANARI (Climate change in the Arctic – North Atlantic region and impacts on the UK), funded by the National Environmental Research Council, UK, under Grant Number NE/W004984/1.

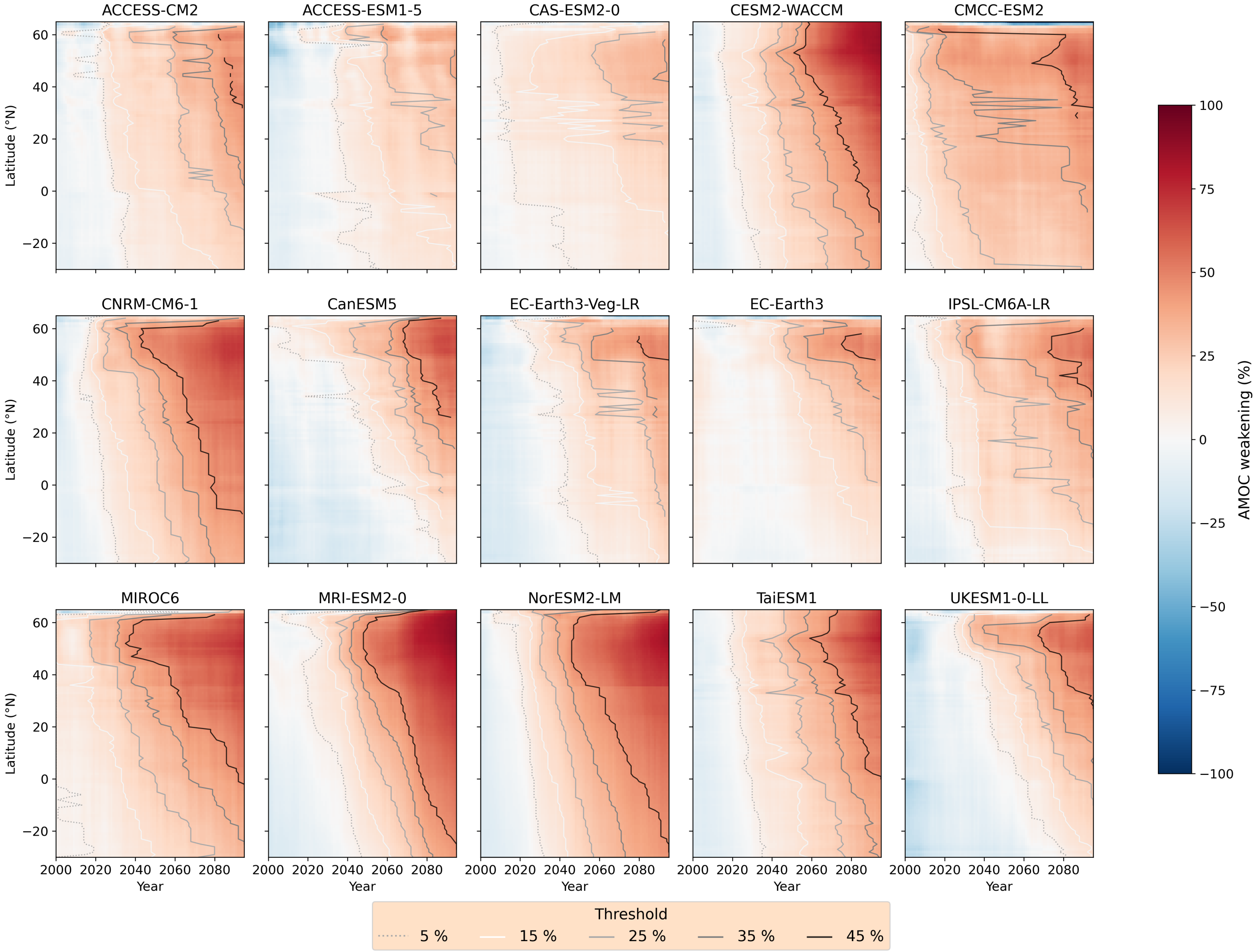

Figure B1. Weakening Hovmöller in density-space for ssp585.

570 ## References

Baker, J. A., Bell, M. J., Jackson, L. C., Renshaw, R., Vallis, G. K., Watson, A. J., and Wood, R. A.: Overturning Pathways Control AMOC Weakening in CMIP6 Models, Geophysical Research Letters, 50, https://doi.org/10.1029/2023GL103381, 2023.

Bellomo, K., Angeloni, M., Corti, S., and von Hardenberg, J.: Future climate change shaped by inter-model differences in Atlantic meridional overturning circulation response, Nature Communications, 12, https://doi.org/10.1038/s41467-021-24015-w, 2021.

575 Bi, D., Dix, M., Marsland, S., O'Farrell, S., Sullivan, A., Bodman, R., Law, R., Harman, I., Srbinovsky, J., Rashid, H. A., Dobrohotoff, P., Mackallah, C., Yan, H., Hirst, A., Savita, A., Dias, F. B., Woodhouse, M., Fiedler, R., and Heerdegen, A.: Configuration and spin-up of ACCESS-CM2, the new generation Australian Community Climate and Earth System Simulator Coupled Model, Journal of Southern Hemisphere Earth Systems Science, 70, 225–251, https://doi.org/10.1071/ES19040, 2020.

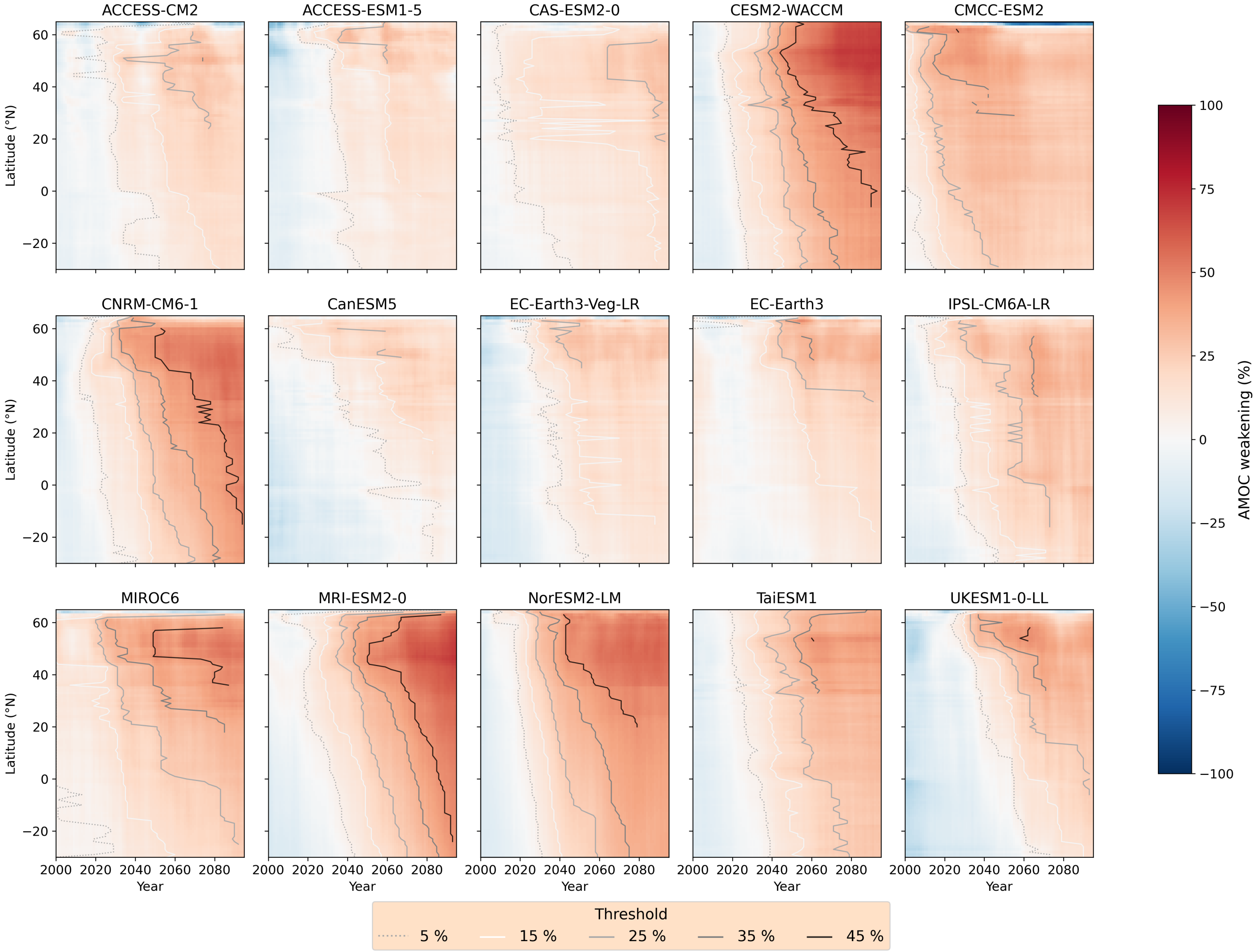

Figure B2. Weakening Hovmöller in density-space for ssp126.

Bonan, D. B., Thompson, A. F., Schneider, T., Zanna, L., Armour, K. C., and Sun, S.: Observational constraints imply limited future Atlantic meridional overturning circulation weakening, Nature Geoscience, 18, 479–487, https://doi.org/10.1038/s41561-025-01709-0, 2025.

Boucher, O., Servonnat, J., Albright, A. L., Aumont, O., Balkanski, Y., Bastrikov, V., Bekki, S., Bonnet, R., Bony, S., Bopp, L., Braconnot, P., Brockmann, P., Cadule, P., Caubel, A., Cheruy, F., Codron, F., Cozic, A., Cugnet, D., D'Andrea, F., Davini, P., de Lavergne, C., Denvil, S., Deshayes, J., Devilliers, M., Ducharne, A., Dufresne, J.-L., Dupont, E., Éthé, C., Fairhead, L., Falletti, L., Flavoni, S., Foujols, M.-A., Gardoll, S., Gastineau, G., Ghattas, J., Grandpeix, J.-Y., Guenet, B., Guez, Lionel, E., Guilyardi, E., Guimberteau, M., Hauglustaine, D., Hourdin, F., Idelkadi, A., Joussaume, S., Kageyama, M., Khodri, M., Krinner, G., Lebas, N., Levavasseur, G., Lévy, C., Li, L., Lott, F., Lurton, T., Luyssaert, S., Madec, G., Madeleine, J.-B., Maignan, F., Marchand, M., Marti, O., Mellul, L., Meurdesoif, Y., Mignot, J., Musat, I., Ottlé, C., Peylin, P., Planton, Y., Polcher, J., Rio, C., Rochetin, N., Rousset, C., Sepulchre, P., Sima, A., Swingedouw, D., Thiéblemont, R., Traore, A. K., Vancoppenolle, M., Vial, J., Vialard, J., Viovy, N., and Vuichard, N.: Presentation and Evaluation of the IPSL-CM6A-

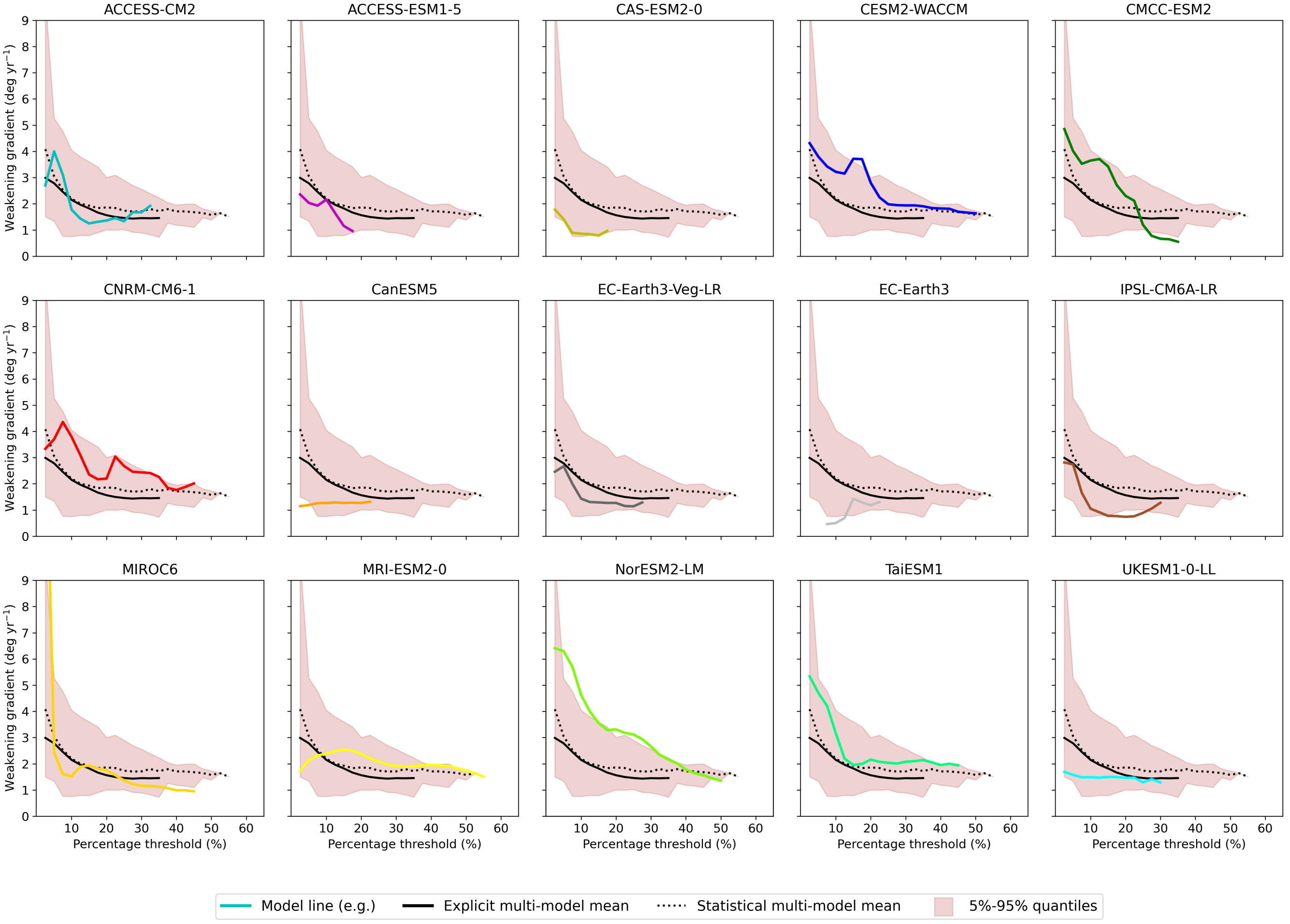

Figure B3. Weakening gradients in density-space for ssp585.

LR Climate Model, Journal of Advances in Modeling Earth Systems, 12, e2019MS002 010, https://doi.org/10.1029/2019MS002010, e2019MS002010 10.1029/2019MS002010, 2020.

Bryden, H., Beunk, J., Drijfhout, S., Hazeleger, W., and Mecking, J.: Comparing observed and modelled components of the Atlantic Meridional Overturning Circulation at 26° N, Ocean Science, 20, 589–599, https://doi.org/10.5194/os-20-589-2024, 2024.

Buckley, M. W., Lozier, M. S., Desbruyères, D., and Evans, D. G.: Buoyancy forcing and the subpolar Atlantic meridional overturning circulation, Philosophical transactions. Series A, Mathematical, physical, and engineering sciences, 381, 20220 181, https://doi.org/10.1098/rsta.2022.0181, 2023.

Danabasoglu, G., Lamarque, J.-F., Bacmeister, J., Bailey, D. A., DuVivier, A. K., Edwards, J., Emmons, L. K., Fasullo, J., Garcia, R., Gettelman, A., Hannay, C., Holland, M. M., Large, W. G., Lauritzen, P. H., Lawrence, D. M., Lenaerts, J. T. M., Lindsay, K., Lipscomb, W. H., Mills, M. J., Neale, R., Oleson, K. W., Otto-Bliesner, B., Phillips, A. S., Sacks, W., Tilmes, S., van Kampenhout, L., Vertenstein, M., Bertini, A., Dennis, J., Deser, C., Fischer, C., Fox-Kemper, B., Kay, J. E., Kinnison, D., Kushner, P. J., Larson, V. E., Long,

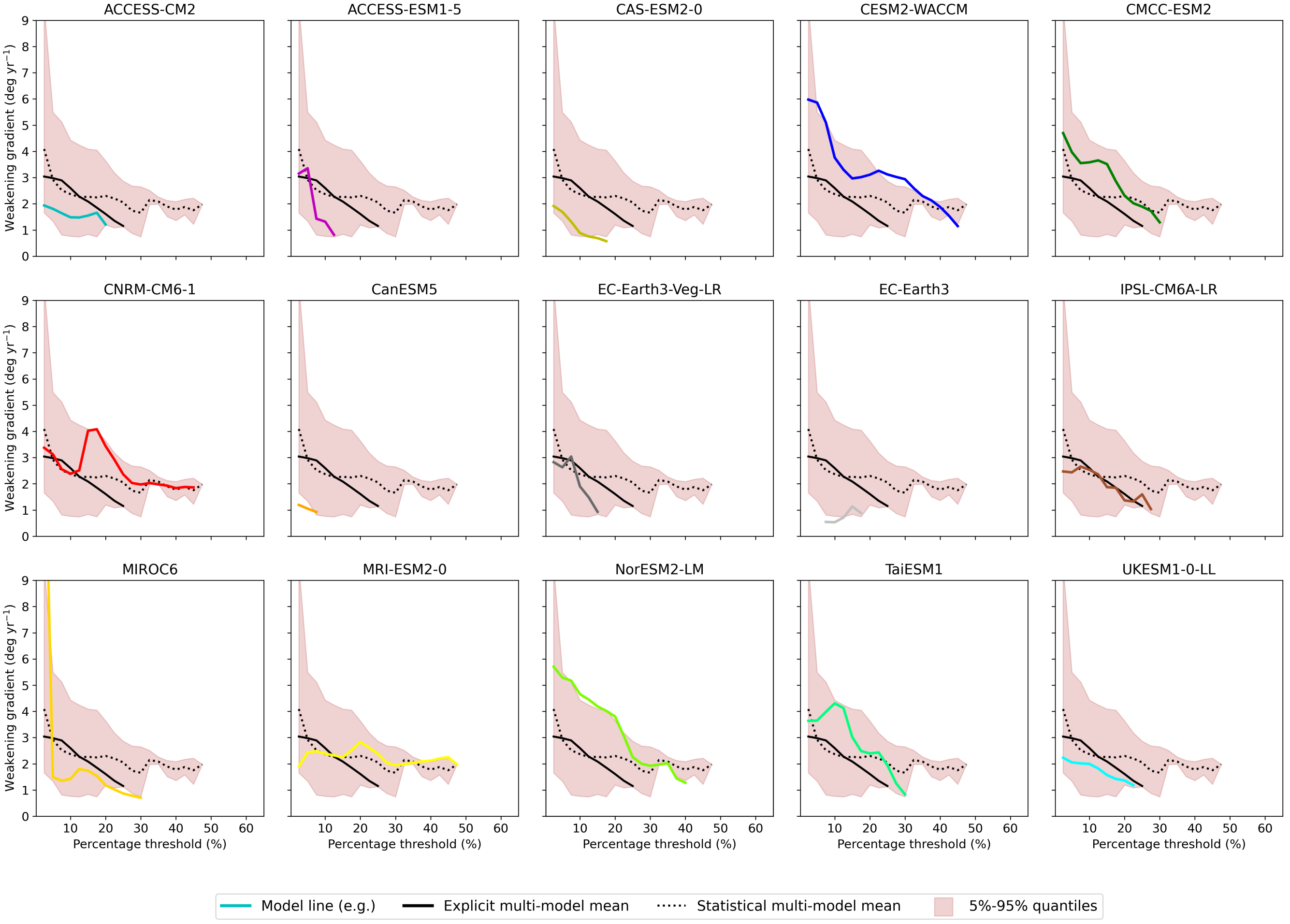

Figure B4. Weakening gradients in density-space for ssp126.

600 M. C., Mickelson, S., Moore, J. K., Nienhouse, E., Polvani, L., Rasch, P. J., and Strand, W. G.: The Community Earth System Model Version 2 (CESM2), Journal of Advances in Modeling Earth Systems, 12, e2019MS001 916, https://doi.org/10.1029/2019MS001916, e2019MS001916 2019MS001916, 2020.

Den Toom, M., Dijkstra, H. A., Weijer, W., Hecht, M. W., Maltrud, M. E., and Van Sebille, E.: Response of a strongly eddying global ocean to North Atlantic freshwater perturbations, Journal of Physical Oceanography, 44, 464–481, https://doi.org/10.1175/JPO-D-12-0155.1, 605 2014.

Dong, B., Aksenov, Y., Colfescu, I., Harvey, B., Hirschi, J., Josey, S., Lu, H., Mecking, J., Oltmanns, M., Osprey, S., Robson, J., Rynders, S., Shaffrey, L., Sinha, B., Sutton, R., and Weisheimer, A.: Key drivers of large scale changes in North Atlantic atmospheric and oceanic circulations and their predictability, Climate Dynamics, 63, https://doi.org/10.1007/s00382-025-07591-1, 2025.

Döscher, R., Böning, C. W., and Herrmann, P.: Response of Circulation and Heat Transport in the North Atlantic to Changes in Thermohaline 610 forcing in Northern Latitudes: A Model Study, Journal of Physical Oceanography, 24, 2306–2320, 1994.

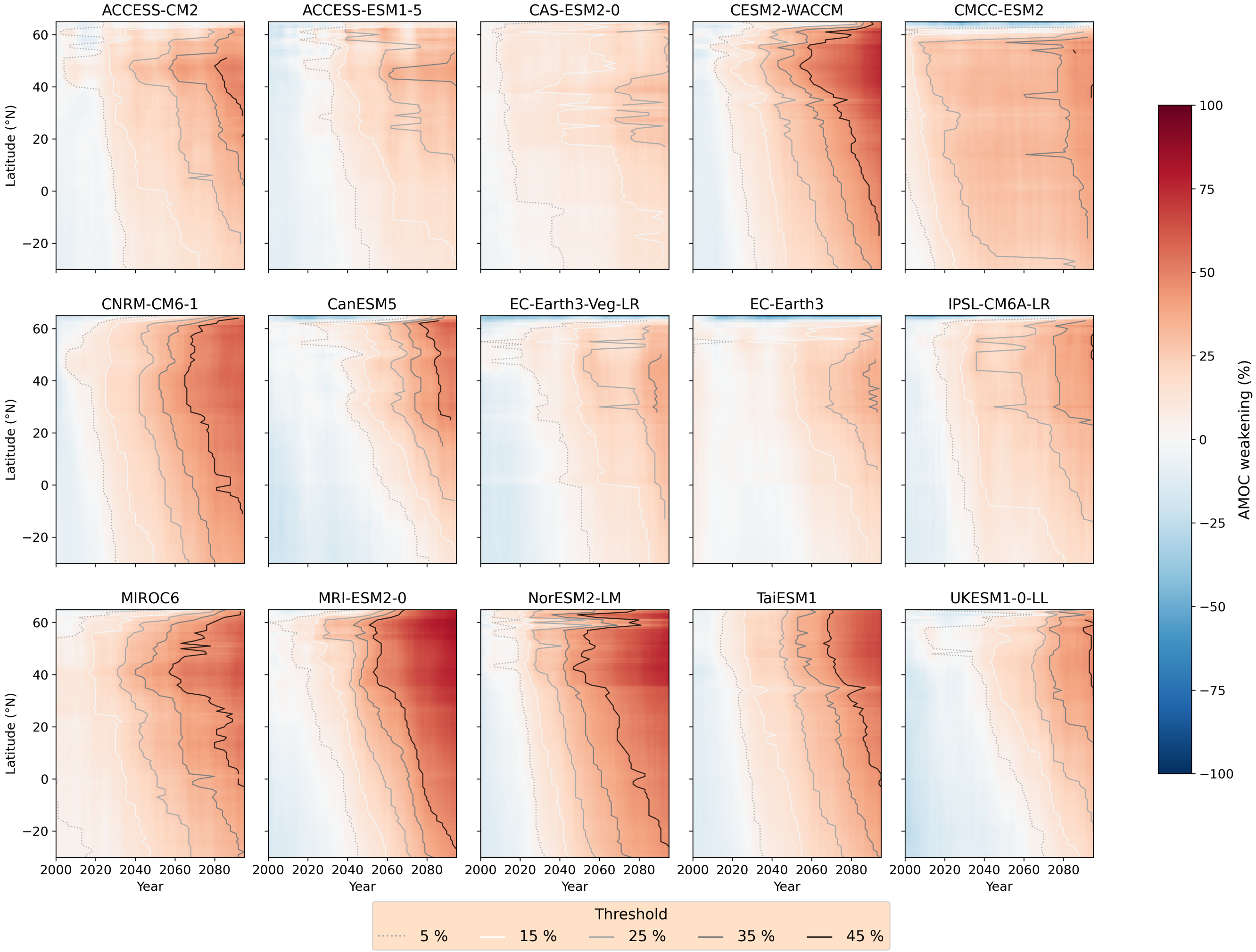

Figure C1. Weakening Hovmöller in depth-space for ssp585.

Döscher, R., Acosta, M., Alessandri, A., Anthoni, P., Arsouze, T., Bergman, T., Bernardello, R., Boussetta, S., Caron, L.-P., Carver, G., Castrillo, M., Catalano, F., Cvijanovic, I., Davini, P., Dekker, E., Doblas-Reyes, F. J., Docquier, D., Echevarria, P., Fladrich, U., Fuentes-Franco, R., Gröger, M., v. Hardenberg, J., Hieronymus, J., Karami, M. P., Keskinen, J.-P., Koenigk, T., Makkonen, R., Massonnet, F., Ménégoz, M., Miller, P. A., Moreno-Chamarro, E., Nieradzik, L., van Noije, T., Nolan, P., O'Donnell, D., Ollinaho, P., van den Oord, 615 G., Ortega, P., Prims, O. T., Ramos, A., Reerink, T., Rousset, C., Ruprich-Robert, Y., Le Sager, P., Schmith, T., Schrödner, R., Serva, F., Sicardi, V., Sloth Madsen, M., Smith, B., Tian, T., Tourigny, E., Uotila, P., Vancoppenolle, M., Wang, S., Wårlind, D., Willén, U., Wyser, K., Yang, S., Yepes-Arbós, X., and Zhang, Q.: The EC-Earth3 Earth system model for the Coupled Model Intercomparison Project 6, Geoscientific Model Development, 15, 2973–3020, https://doi.org/10.5194/gmd-15-2973-2022, 2022.

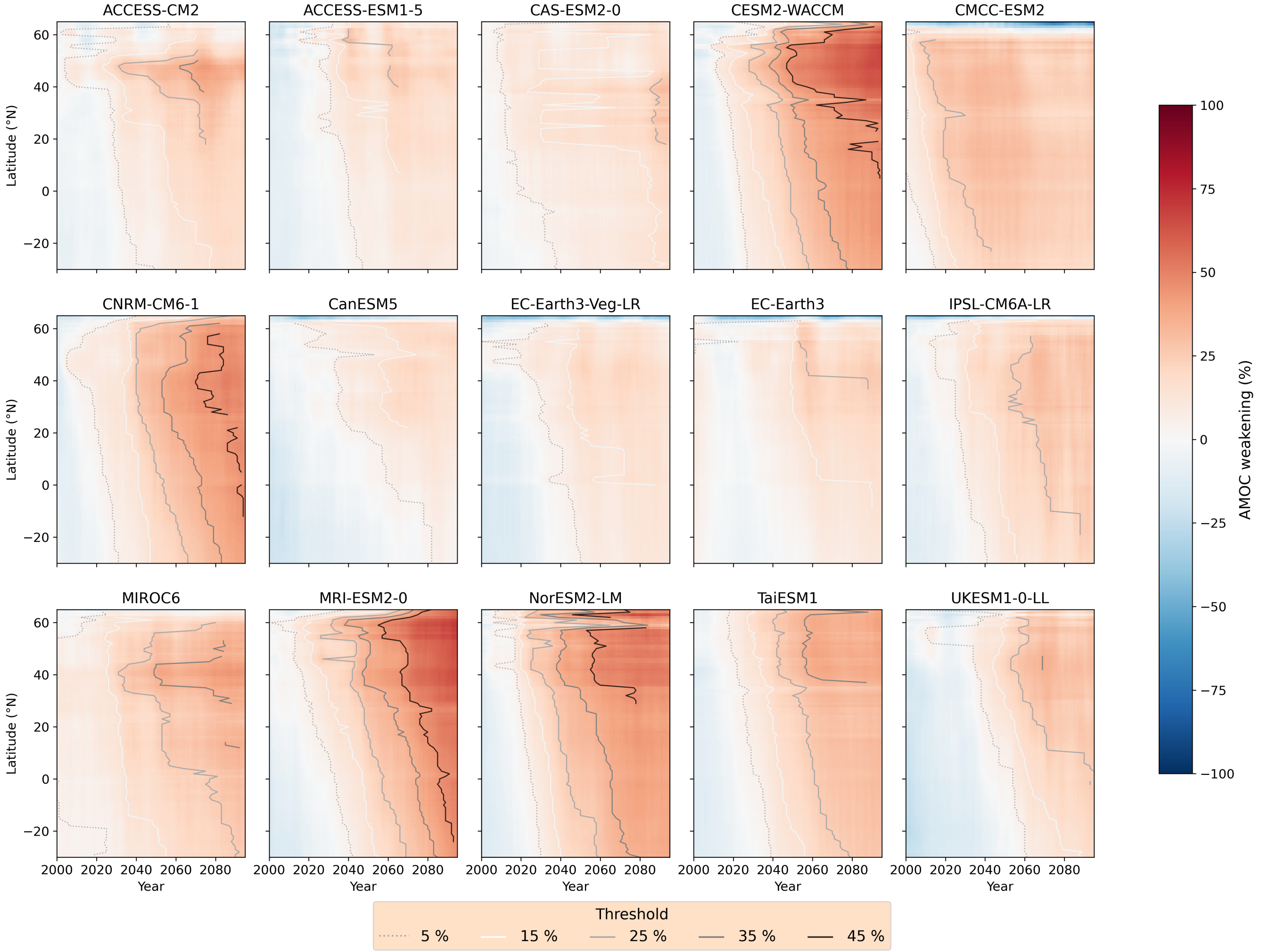

Figure C2. Weakening Hovmöller in depth-space for ssp126.

Drijfhout, S., Angevaare, J. R., Mecking, J., van Westen, R. M., and Rahmstorf, S.: Shutdown of northern Atlantic overturning after 2100 following deep mixing collapse in CMIP6 projections, Environmental Research Letters, 20, https://doi.org/10.1088/1748-9326/adfa3b, 2025.

Duarte, D., Liu, W., and Zhang, L.: A weakened Atlantic Meridional Overturning Circulation will affect future heat waves by mostly attenuating their severity, Climate Dynamics, 63, https://doi.org/10.1007/s00382-025-07736-2, 2025.

Eyring, V., Bony, S., Meehl, G. A., Senior, C. A., Stevens, B., Stouffer, R. J., and Taylor, K. E.: Overview of the Coupled Model Intercomparison Project Phase 6 (CMIP6) experimental design and organization, Geoscientific Model Development, 9, 1937–1958, https://doi.org/10.5194/gmd-9-1937-2016, 2016.

Fox-Kemper, B., Hewitt, H., Xiao, C., Aðalgeirsdóttir, G., Drijfhout, S., Edwards, T., Golledge, N., Hemer, M., Kopp, R., Krinner, G., Mix, A., Notz, D., Nowicki, S., Nurhati, I., Ruiz, L., Sallée, J.-B., Slangen, A., and Yu, Y.: Ocean, Cryosphere and Sea Level Change, in: Climate

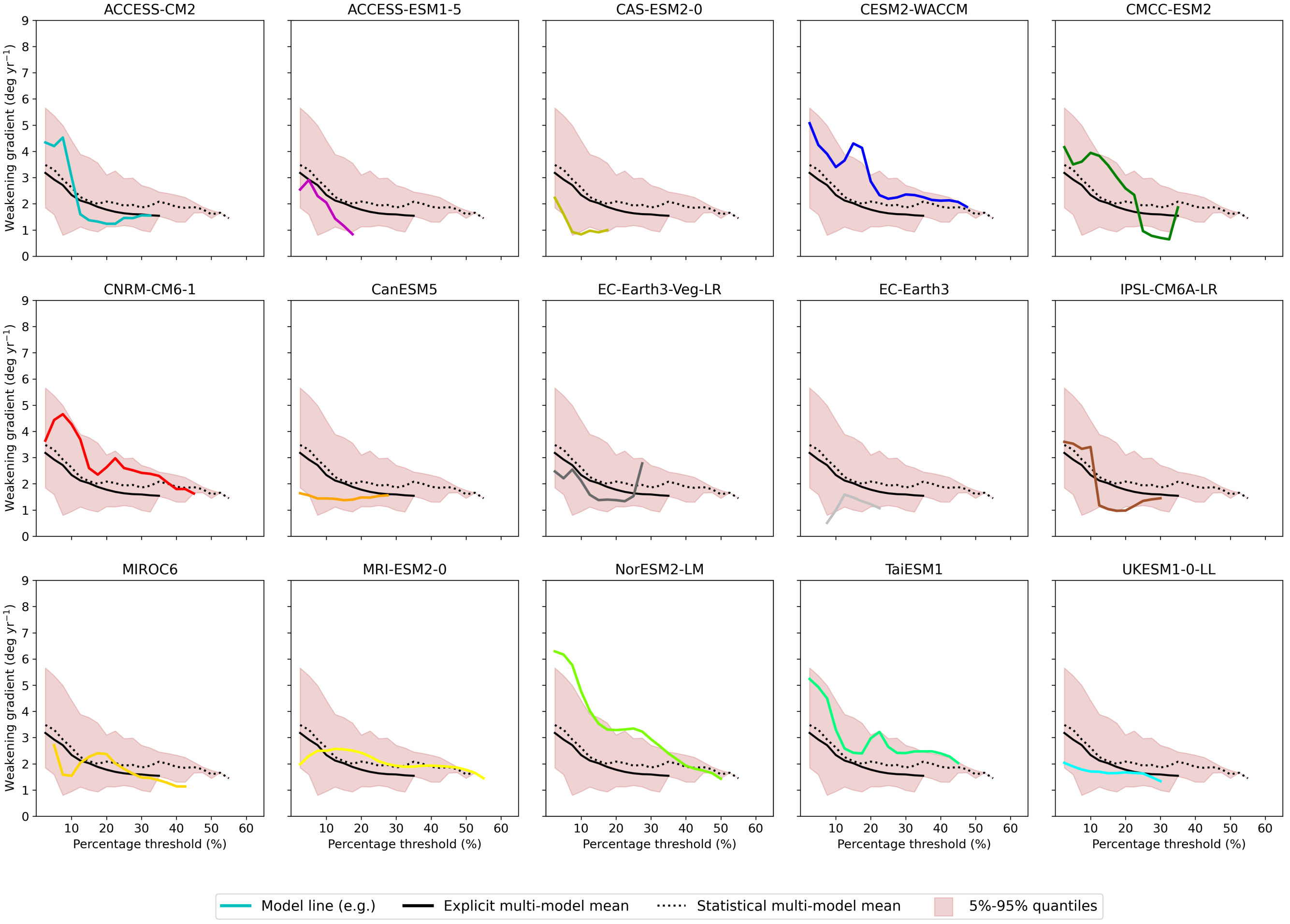

Figure C3. Weakening gradients in depth-space for ssp585.

Change 2021 – The Physical Science Basis, pp. 1211–1362, Cambridge University Press, https://doi.org/10.1017/9781009157896.011, 2021. 630

Fraser, N. J., Fox, A. D., and Cunningham, S. A.: Impact of Ekman Pumping on the Meridional Coherence of the AMOC, Geophysical Research Letters, 52, https://doi.org/10.1029/2024GL108846, 2025.

Gerdes, R. and Köberle, C.: On the Influence of DSOW in a Numerical Model of the North Atlantic General Circulation, Journal of Physical Oceanography, 25, 2624–2642, 1995.

635 Gu, S., Liu, Z., and Wu, L.: Time Scale Dependence of the Meridional Coherence of the Atlantic Meridional Overturning Circulation, Journal of Geophysical Research: Oceans, 125, https://doi.org/10.1029/2019JC015838, 2020.

Han, L.: Exploring the AMOC Connectivity Between the RAPID and OSNAP Lines With a Model-Based Data Set, Geophysical Research Letters, 50, https://doi.org/10.1029/2023GL105225, 2023.

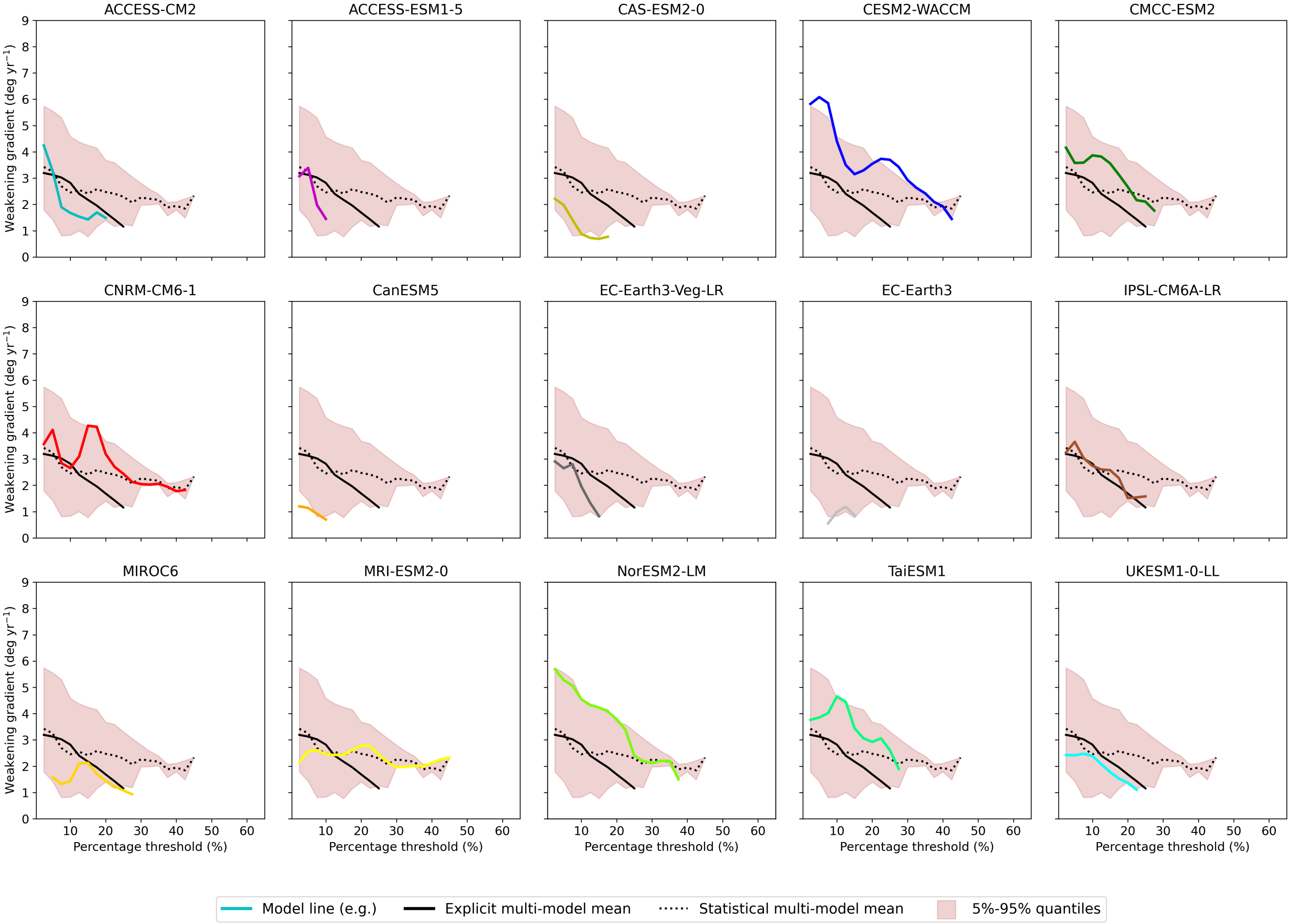

Figure C4. Weakening gradients in depth-space for ssp126.

Hirschi, J. and Marotzke, J.: Reconstructing the meridional overturning circulation from boundary densities and the zonal wind stress, Journal of Physical Oceanography, 37, 743–763, https://doi.org/10.1175/JPO3019.1, 2007. 640

Hirschi, J. J., Barnier, B., Böning, C., Biastoch, A., Blaker, A. T., Coward, A., Danilov, S., Drijfhout, S., Getzlaff, K., Griffies, S. M., Hasumi, H., Hewitt, H., Iovino, D., Kawasaki, T., Kiss, A. E., Koldunov, N., Marzocchi, A., Mecking, J. V., Moat, B., Molines, J. M., Myers, P. G., Penduff, T., Roberts, M., Treguier, A. M., Sein, D. V., Sidorenko, D., Small, J., Spence, P., Thompson, L. A., Weijer, W., and Xu, X.: The Atlantic Meridional Overturning Circulation in High-Resolution Models, Journal of Geophysical Research: Oceans, 125, https://doi.org/10.1029/2019JC015522, 2020. 645

Hodson, D. L. and Sutton, R. T.: The impact of resolution on the adjustment and decadal variability of the Atlantic meridional overturning circulation in a coupled climate model, Climate Dynamics, 39, 3057–3073, https://doi.org/10.1007/s00382-012-1309-0, 2012.

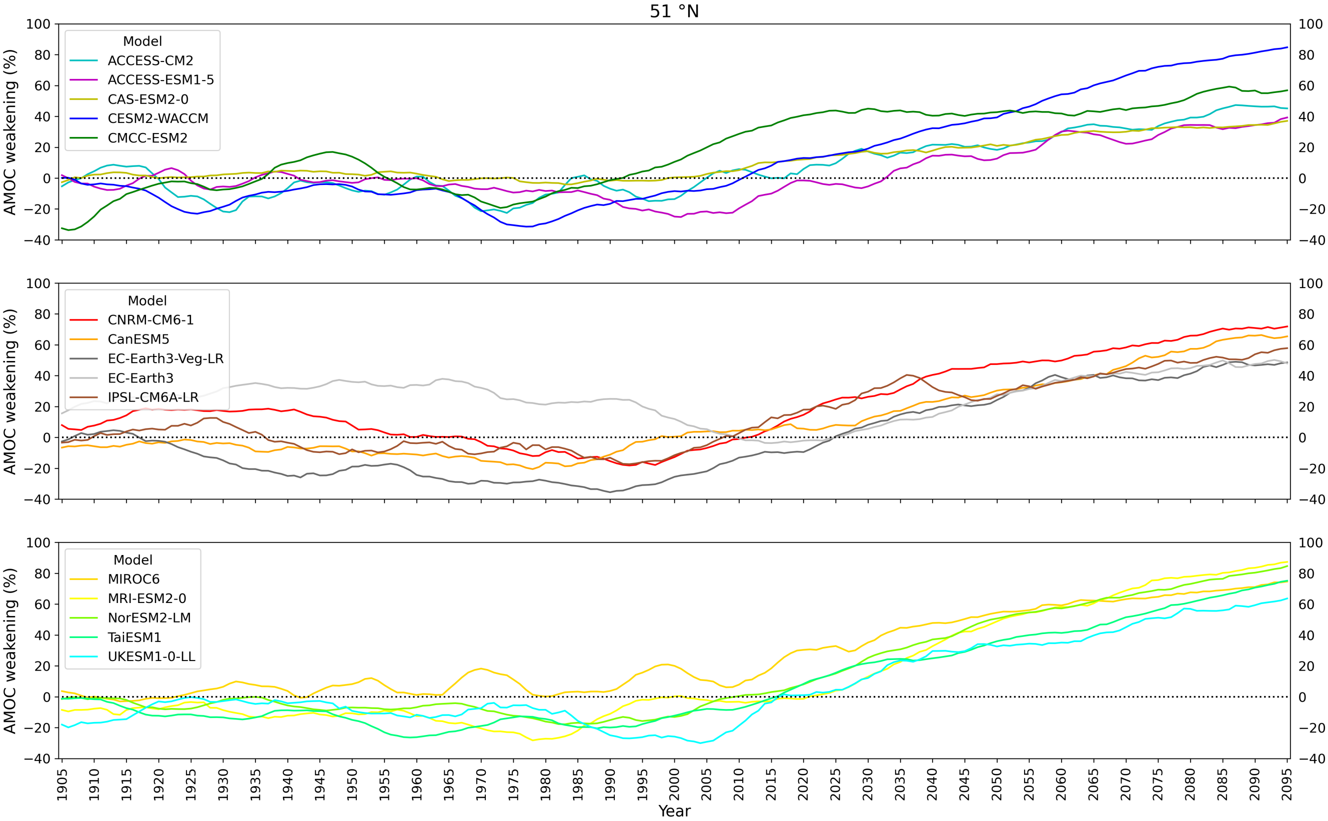

Figure D1. Timeseries of relative AMOC strength for the model set under historical and ssp585 forcing at 51°N, relative to the mean 1850-1899 strength. The models are separated into groups of 5 for visual clarity.

IOC, SCOR, and IAPSO: The international thermodynamic equation of seawater-2010: Calculation and use of thermodynamic properties Intergovernmental Oceanographic Commission, Intergovernmental Oceanographic Commission, Manuals and Guides No. 56, UNESCO (English), 196 pp., 2010.

Jackson, L. C. and Wood, R. A.: Fingerprints for early detection of changes in the AMOC, Journal of Climate, 33, 7027–7044, https://doi.org/10.1175/JCLI-D-20-0034.1, 2020.

Jackson, L. C., Kahana, R., Graham, T., Ringer, M. A., Woollings, T., Mecking, J. V., and Wood, R. A.: Global and European climate impacts of a slowdown of the AMOC in a high resolution GCM, Climate Dynamics, 45, 3299–3316, https://doi.org/10.1007/s00382-015-2540-2, 2015.

Jackson, L. C., Roberts, M. J., Hewitt, H. T., Iovino, D., Koenigk, T., Meccia, V. L., Roberts, C. D., Ruprich-Robert, Y., and Wood, R. A.: Impact of ocean resolution and mean state on the rate of AMOC weakening, Climate Dynamics, 55, 1711–1732, https://doi.org/10.1007/s00382-020-05345-9, 2020.

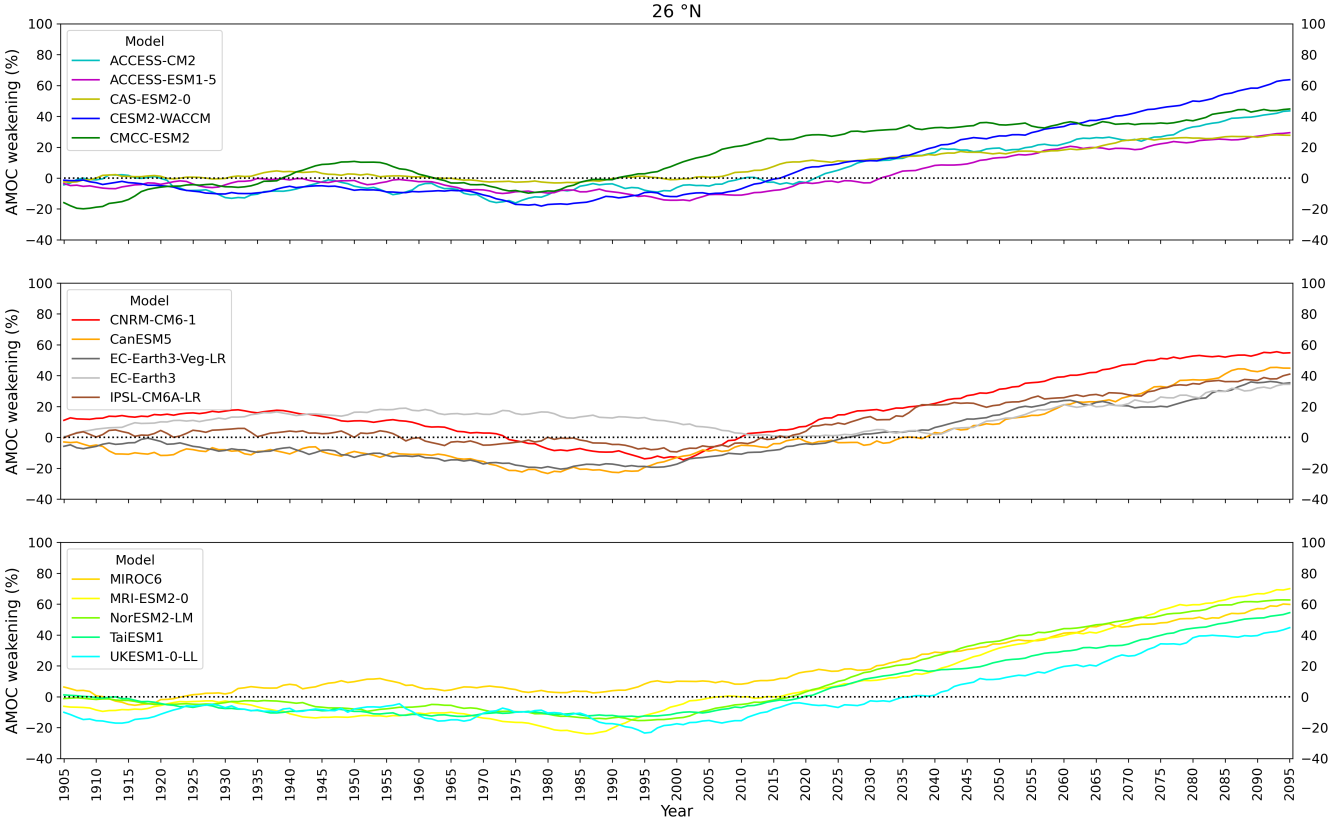

Figure D2. Timeseries of relative AMOC strength for the model set under historical and ssp585 forcing at 26°N, relative to the mean 1850-1899 strength. The models are separated into groups of 5 for visual clarity.

Jackson, L. C., Biastoch, A., Buckley, M. W., Desbruyères, D. G., Frajka-Williams, E., Moat, B., and Robson, J.: The evolution of the North Atlantic Meridional Overturning Circulation since 1980, Nature Reviews Earth and Environment, 3, 241–254, https://doi.org/10.1038/s43017-022-00263-2, 2022.

Johns, W. E., Elipot, S., Smeed, D. A., Moat, B., King, B., Volkov, D. L., and Smith, R. H.: Towards two decades of Atlantic Ocean mass and heat transports at 26.5° N, Philosophical transactions. Series A, Mathematical, physical, and engineering sciences, 381, 20220 188, https://doi.org/10.1098/rsta.2022.0188, 2023.

Kostov, Y., Messias, M. J., Mercier, H., Johnson, H. L., and Marshall, D. P.: Fast mechanisms linking the Labrador Sea with subtropical Atlantic overturning, Climate Dynamics, 60, 2687–2712, https://doi.org/10.1007/s00382-022-06459-y, 2022.

Kwon, Y. O. and Frankignoul, C.: Mechanisms of multidecadal atlantic meridional overturning circulation variability diagnosed in depth versus density space, Journal of Climate, 27, 9359–9376, https://doi.org/10.1175/JCLI-D-14-00228.1, 2014.

Levang, S. J. and Schmitt, R. W.: What causes the AMOC to weaken in CMIP5?, Journal of Climate, 33, 1535–1545, https://doi.org/10.1175/JCLI-D-19-0547.1, 2020.

Li, F., Susan Lozier, M., Danabasoglu, G., Holliday, N. P., Kwon, Y.-o., Romanou, A., Yeager, S. G., and Zhang, R.: Local and Downstream Relationships between Labrador Sea Water Volume and North Atlantic Meridional Overturning Circulation Variability, Journal of Climate, 32, 3883–3898, https://doi.org/10.1175/JCLI-D-18, 2019.

Li, F., Lozier, M. S., Bacon, S., Bower, A. S., Cunningham, S. A., de Jong, M. F., deYoung, B., Fraser, N., Fried, N., Han, G., Holliday, N. P., Holte, J., Houpert, L., Inall, M. E., Johns, W. E., Jones, S., Johnson, C., Karstensen, J., Le Bras, I. A., Lherminier, P., Lin, X., Mercier, H., Oltmanns, M., Pacini, A., Petit, T., Pickart, R. S., Rayner, D., Straneo, F., Thierry, V., Visbeck, M., Yashayaev, I., and Zhou, C.: Subpolar North Atlantic western boundary density anomalies and the Meridional Overturning Circulation, Nature Communications, 12, https://doi.org/10.1038/s41467-021-23350-2, 2021.

Lin, Y.-J., Rose, B. E. J., and Hwang, Y.-T.: Mean State AMOC Affects AMOC Weakening through Subsurface Warming in the Labrador Sea, Journal of Climate, 36, 3895, https://doi.org/10.1175/JCLI-D-22-0464.1, 2023.

Liu, W., Fedorov, A. V., Xie, S.-P., and Hu, S.: Climate impacts of a weakened Atlantic Meridional Overturning Circulation in a warming climate, Science Advances, https://www.science.org, 2020.

Lobelle, D., Beaulieu, C., Livina, V., Sévellec, F., and Frajka-Williams, E.: Detectability of an AMOC Decline in Current and Projected Climate Changes, Geophysical Research Letters, 47, https://doi.org/10.1029/2020GL089974, 2020.

Lovato, T., Peano, D., Butenschön, M., Materia, S., Iovino, D., Scoccimarro, E., Fogli, P. G., Cherchi, A., Bellucci, A., Gualdi, S., Masina, S., and Navarra, A.: CMIP6 Simulations With the CMCC Earth System Model (CMCC-ESM2), Journal of Advances in Modeling Earth Systems, 14, e2021MS002 814, https://doi.org/10.1029/2021MS002814, e2021MS002814 2021MS002814, 2022.

Lozier, M. S., Bacon, S., Bower, A. S., Cunningham, S. A., De Jong, M. F., De Steur, L., De Young, B., Fischer, J., Gary, S. F., Greenan, B. J., Heimbmbach, P., Holliday, N. P., Houpert, L., Inall, M. E., Johns, W. E., Johnson, H. L., Karstensen, J., Li, F., Lin, X., Mackay, N., Marshall, D. P., Mercier, H., Myers, P. G., Pickart, R. S., Pillar, H. R., Straneo, F., Thierry, V., Weller, R. A., Williams, R. G., Wilson, C., Yang, J., Zhao, J., and Zika, J. D.: Overturning in the Subpolar north Atlantic program: A new international ocean observing system, Bulletin of the American Meteorological Society, 98, 737–752, https://doi.org/10.1175/BAMS-D-16-0057.1, 2017.

Madan, G., Gjermundsen, A., Iversen, S. C., and LaCasce, J. H.: The weakening AMOC under extreme climate change, Climate Dynamics, https://doi.org/10.1007/s00382-023-06957-7, 2023.

Marshall, D. P. and Johnson, H. L.: Propagation of meridional circulation anomalies along western and eastern boundaries, Journal of Physical Oceanography, 43, 2699–2717, https://doi.org/10.1175/JPO-D-13-0134.1, 2013.

McDougall, T. J. and Barker, P. M.: Getting started with TEOS-10 and the Gibbs Seawater (GSW) Oceanographic Toolbox, SCOR/IAPSO WG127, ISBN 978-0-646-55621-5, 2011.

Meccia, V. L., Simolo, C., Bellomo, K., and Corti, S.: The impact of a weakened AMOC on European heatwaves, Environmental Research Letters, 20, 024 005, https://doi.org/10.1088/1748-9326/ada3e7, 2025.

Menary, M. B., Robson, J., Allan, R. P., Booth, B. B., Cassou, C., Gastineau, G., Gregory, J., Hodson, D., Jones, C., Mignot, J., Ringer, M., Sutton, R., Wilcox, L., and Zhang, R.: Aerosol-Forced AMOC Changes in CMIP6 Historical Simulations, Geophysical Research Letters, 47, https://doi.org/10.1029/2020GL088166, 2020.

O'Neill, B. C., Tebaldi, C., Van Vuuren, D. P., Eyring, V., Friedlingstein, P., Hurtt, G., Knutti, R., Kriegler, E., Lamarque, J. F., Lowe, J., Meehl, G. A., Moss, R., Riahi, K., and Sanderson, B. M.: The Scenario Model Intercomparison Project (ScenarioMIP) for CMIP6, Geoscientific Model Development, 9, 3461–3482, https://doi.org/10.5194/gmd-9-3461-2016, 2016.

Ortega, P., Robson, J. I., Menary, M., Sutton, R. T., Blaker, A., Germe, A., Hirschi, J. J., Sinha, B., Hermanson, L., and Yeager, S.: Labrador Sea subsurface density as a precursor of multidecadal variability in the North Atlantic: A multi-model study, Earth System Dynamics, 12, 419–438, https://doi.org/10.5194/esd-12-419-2021, 2021.

Petit, T., Robson, J., Ferreira, D., Yeager, S., and Evans, D. G.: Coherence of the AMOC Over the Subpolar North Atlantic on Interannual to Multiannual Time Scales, Geophysical Research Letters, 52, https://doi.org/10.1029/2025GL115171, 2025.

Pickart, R. S. and Spall, M. A.: Impact of Labrador Sea convection on the North Atlantic meridional overturning circulation, Journal of Physical Oceanography, 37, 2207–2227, https://doi.org/10.1175/JPO3178.1, 2007.

Pita, I., Elipot, S., Johns, W., Smeed, D., and Moat, B.: Changing properties of NADW cause AMOC weakening at 26.5°N, EGU General Assembly 2025, Vienna, Austria, 27 Apr–2 May 2025, EGU25-19557, https://doi.org/10.5194/egusphere-egu25-19557, 2025.

Robson, J., Menary, M. B., Sutton, R. T., Mecking, J., Gregory, J. M., Jones, C., Sinha, B., Stevens, D. P., and Wilcox, L. J.: The Role of Anthropogenic Aerosol Forcing in the 1850-1985 Strengthening of the AMOC in CMIP6 Historical Simulations, Journal of Climate, 35, 6843, https://doi.org/10.1175/JCLI-D-22-0124.1, 2022.

Seland, Ø., Bentsen, M., Olivié, D., Toniazzo, T., Gjermundsen, A., Graff, L. S., Debernard, J. B., Gupta, A. K., He, Y.-C., Kirkevåg, A., Schwinger, J., Tjiputra, J., Aas, K. S., Bethke, I., Fan, Y., Griesfeller, J., Grini, A., Guo, C., Ilicak, M., Karset, I. H. H., Landgren, O., Liakka, J., Moseid, K. O., Nummelin, A., Spensberger, C., Tang, H., Zhang, Z., Heinze, C., Iversen, T., and Schulz, M.: Overview of the Norwegian Earth System Model (NorESM2) and key climate response of CMIP6 DECK, historical, and scenario simulations, Geoscientific Model Development, 13, 6165–6200, https://doi.org/10.5194/gmd-13-6165-2020, 2020.

Sellar, A. A., Jones, C. G., Mulcahy, J. P., Tang, Y., Yool, A., Wiltshire, A., O'Connor, F. M., Stringer, M., Hill, R., Palmieri, J., Woodward, S., de Mora, L., Kuhlbrodt, T., Rumbold, S. T., Kelley, D. I., Ellis, R., Johnson, C. E., Walton, J., Abraham, N. L., Andrews, M. B., Andrews, T., Archibald, A. T., Berthou, S., Burke, E., Blockley, E., Carslaw, K., Dalvi, M., Edwards, J., Folberth, G. A., Gedney, N., Griffiths, P. T., Harper, A. B., Hendry, M. A., Hewitt, A. J., Johnson, B., Jones, A., Jones, C. D., Keeble, J., Liddicoat, S., Morgenstern, O., Parker, R. J., Predoi, V., Robertson, E., Siahaan, A., Smith, R. S., Swaminathan, R., Woodhouse, M. T., Zeng, G., and Zerroukat, M.: UKESM1: Description and Evaluation of the U.K. Earth System Model, Journal of Advances in Modeling Earth Systems, 11, 4513–4558, https://doi.org/10.1029/2019MS001739, 2019.

Smeed, D. A., McCarthy, G. D., Cunningham, S. A., Frajka-Williams, E., Rayner, D., Johns, W. E., Meinen, C. S., Baringer, M. O., Moat, B. I., Duchez, A., and Bryden, H. L.: Observed decline of the Atlantic meridional overturning circulation 2004-2012, https://doi.org/10.5194/os-10-29-2014, 2014.

Straneo, F.: On the Connection between Dense Water Formation, Overturning, and Poleward Heat Transport in a Convective Basin*, Journal of Physical Oceanography, 36, 1822–1840, 2006.

Swart, N. C., Cole, J. N. S., Kharin, V. V., Lazare, M., Scinocca, J. F., Gillett, N. P., Anstey, J., Arora, V., Christian, J. R., Hanna, S., Jiao, Y., Lee, W. G., Majaess, F., Saenko, O. A., Seiler, C., Seinen, C., Shao, A., Sigmond, M., Solheim, L., von Salzen, K., Yang, D., and Winter, B.: The Canadian Earth System Model version 5 (CanESM5.0.3), Geoscientific Model Development, 12, 4823–4873, https://doi.org/10.5194/gmd-12-4823-2019, 2019.

Tatebe, H., Ogura, T., Nitta, T., Komuro, Y., Ogochi, K., Takemura, T., Sudo, K., Sekiguchi, M., Abe, M., Saito, F., Chikira, M., Watanabe, S., Mori, M., Hirota, N., Kawatani, Y., Mochizuki, T., Yoshimura, K., Takata, K., O'ishi, R., Yamazaki, D., Suzuki, T., Kurogi, M., Kataoka, T., Watanabe, M., and Kimoto, M.: Description and basic evaluation of simulated mean state, internal variability, and climate sensitivity in MIROC6, Geoscientific Model Development, 12, 2727–2765, https://doi.org/10.5194/gmd-12-2727-2019, 2019.

Tooth, O.: NOC-MSM/nemo_cookbook:v2026.01.0b1 (v2026.01.0b1), Zenodo, https://doi.org/10.5281/zenodo.18292769, 2026.

Trenberth, K. E. and Fasullo, J. T.: Atlantic meridional heat transports computed from balancing Earth's energy locally, Geophysical Research Letters, 44, 1919–1927, https://doi.org/10.1002/2016GL072475, 2017.

Vacca, A. V., Bellomo, K., Fabiano, F., and von Hardenberg, J.: On the role of AMOC weakening in shaping wintertime Euro-Atlantic atmospheric circulation, Climate Dynamics, 63, https://doi.org/10.1007/s00382-025-07747-z, 2025.

van Westen, R. M. and Baatsen, M. L.: European Temperature Extremes Under Different AMOC Scenarios in the Community Earth System Model, Geophysical Research Letters, 52, https://doi.org/10.1029/2025GL114611, 2025.

van Westen, R. M., Kliphuis, M., and Dijkstra, H. A.: Collapse of the Atlantic Meridional Overturning Circulation in a Strongly Eddying Ocean-Only Model, Geophysical Research Letters, 52, https://doi.org/10.1029/2024GL114532, 2025.

Voldoire, A., Saint-Martin, D., Sénési, S., Decharme, B., Alias, A., Chevallier, M., Colin, J., Guérémy, J.-F., Michou, M., Moine, M.-P., Nabat, P., Roehrig, R., Salas y Mélia, D., Séférian, R., Valcke, S., Beau, I., Belamari, S., Berthet, S., Cassou, C., Cattiaux, J., Deshayes, J., Douville, H., Ethé, C., Franchistéguy, L., Geoffroy, O., Lévy, C., Madec, G., Meurdesoif, Y., Msadek, R., Ribes, A., Sanchez-Gomez, E., Terray, L., and Waldman, R.: Evaluation of CMIP6 DECK Experiments With CNRM-CM6-1, Journal of Advances in Modeling Earth Systems, 11, 2177–2213, https://doi.org/10.1029/2019MS001683, 2019.

Wang, Y.-C., Hsu, H.-H., Chen, C.-A., Tseng, W.-L., Hsu, P.-C., Lin, C.-W., Chen, Y.-L., Jiang, L.-C., Lee, Y.-C., Liang, H.-C., Chang, W.-M., Lee, W.-L., and Shiu, C.-J.: Performance of the Taiwan Earth System Model in Simulating Climate Variability Compared With Observations and CMIP6 Model Simulations, Journal of Advances in Modeling Earth Systems, 13, e2020MS002 353, https://doi.org/10.1029/2020MS002353, e2020MS002353 2020MS002353, 2021.

Weijer, W., Maltrud, M. E., Hecht, M. W., Dijkstra, H. A., and Kliphuis, M. A.: Response of the Atlantic Ocean circulation to Greenland Ice Sheet melting in a strongly-eddying ocean model, https://doi.org/10.1029/2012GL051611, 2012.

Weijer, W., Cheng, W., Garuba, O. A., Hu, A., and Nadiga, B. T.: CMIP6 Models Predict Significant 21st Century Decline of the Atlantic Meridional Overturning Circulation, Geophysical Research Letters, 47, https://doi.org/10.1029/2019GL086075, 2020.

Wett, S., Rhein, M., Kieke, D., Mertens, C., and Moritz, M.: Meridional Connectivity of a 25-Year Observational AMOC Record at 47°N, Geophysical Research Letters, 50, https://doi.org/10.1029/2023GL103284, 2023.

Yukimoto, S., Kawai, H., Koshiro, T., Oshima, N., Yoshida, K., Urakawa, S., Tsujino, H., Deushi, M., Tanaka, T., Hosaka, M., Yabu, S., Yoshimura, H., Shindo, E., Mizuta, R., Obata, A., Adachi, Y., and Ishii, M.: The Meteorological Research Institute Earth System Model Version 2.0, MRI-ESM2.0: Description and Basic Evaluation of the Physical Component, Journal of the Meteorological Society of Japan. Ser. II, 97, 931–965, https://doi.org/10.2151/jmsj.2019-051, 2019.

Zhang, H., Zhang, M., Jin, J., Fei, K., Ji, D., Wu, C., Zhu, J., He, J., Chai, Z., Xie, J., Dong, X., Zhang, D., Bi, X., Cao, H., Chen, H., Chen, K., Chen, X., Gao, X., Hao, H., Jiang, J., Kong, X., Li, S., Li, Y., Lin, P., Lin, Z., Liu, H., Liu, X., Shi, Y., Song, M., Wang, H., Wang, T., Wang, X., Wang, Z., Wei, Y., Wu, B., Xie, Z., Xu, Y., Yu, Y., Yuan, L., Zeng, Q., Zeng, X., Zhao, S., Zhou, G., and Zhu, J.: Description and Climate Simulation Performance of CAS-ESM Version 2, Journal of Advances in Modeling Earth Systems, 12, e2020MS002 210, https://doi.org/10.1029/2020MS002210, e2020MS002210 2020MS002210, 2020.

Zhang, R.: Latitudinal dependence of Atlantic meridional overturning circulation (AMOC) variations, Geophysical Research Letters, 37, https://doi.org/10.1029/2010GL044474, 2010.

Zhao, A., Robson, J., Sutton, R., Lai, M. W., Mecking, J. V., Yeager, S., and Petit, T.: Large diversity in AMOC internal variability across NEMO-based climate models, Climate Dynamics, 62, 3355–3374, https://doi.org/10.1007/s00382-023-07069-y, 2024.

Zhao, B., Reichler, T., Strong, C., and Penland, C.: Simultaneous evolution of gyre and Atlantic meridional overturning circulation anomalies as an eigenmode of the North Atlantic system, Journal of Climate, 30, 6737–6755, https://doi.org/10.1175/JCLI-D-16-0751.1, 2017.

Ziehn, T., Chamberlain, M. A., Law, R. M., Lenton, A., Bodman, R. W., Dix, M., Stevens, L., Wang, Y.-P., and Srbinovsky, J.: The Australian Earth System Model: ACCESS-ESM1.5, Journal of Southern Hemisphere Earth Systems Science, 70, 193–214, https://doi.org/https://doi.org/10.1071/ES19035, 2020. 785

Zou, S., Lozier, M. S., and Buckley, M.: How Is Meridional Coherence Maintained in the Lower Limb of the Atlantic Meridional Overturning Circulation?, Geophysical Research Letters, 46, 244–252, https://doi.org/10.1029/2018GL080958, 2019.